










# Resolved Molecular Gas Observations of MaNGA Post-starbursts Reveal a Tumultuous Past

Justin Atsushi Otter<sup>1</sup> , Kate Rowlands<sup>1,2</sup> , Katherine Alatalo<sup>1,3</sup> , Ho-Hin Leung<sup>4</sup> , Vivienne Wild<sup>4</sup> , Yuanze Luo<sup>1</sup> , Andreea O. Petric<sup>3</sup> , Elizaveta Sazonova<sup>1,5,6</sup> , David V. Stark<sup>3,7</sup> , Timothy Heckman<sup>1</sup> , Timothy A. Davis<sup>8</sup> , Sara Ellison<sup>9</sup> , K. Decker French<sup>10</sup> , William Baker<sup>11,12</sup> , Asa F. L. Bluck<sup>13</sup> , Lauranne Lanz<sup>14</sup> , Lihwai Lin<sup>15</sup> , Charles Liu<sup>16,17,18</sup> , Carlos López Cobá<sup>15</sup> , Karen L. Masters<sup>7</sup> , Preethi Nair<sup>19</sup> , Hsi-an Pan (潘璽安)<sup>20</sup> , Rogemar A. Riffel<sup>21,22</sup> , Jillian M. Scudder<sup>23</sup> , Adam Smercina<sup>24</sup> , Freeke van de Voort<sup>8</sup> , and John R. Weaver<sup>25,26,27</sup> 

<sup>1</sup> William H. Miller III Department of Physics and Astronomy, Johns Hopkins University, Baltimore, MD 21218, USA; [jotter2@jhu.edu](mailto:jotter2@jhu.edu)

<sup>2</sup> AURA for ESA, Space Telescope Science Institute, 3700 San Martin Drive, Baltimore, MD 21218, USA

<sup>3</sup> Space Telescope Science Institute, 3700 San Martin Drive, Baltimore, MD 21218, USA

<sup>4</sup> SUPA, School of Physics & Astronomy, University of St Andrews, North Haugh, St Andrews, Fife KY16 9SS, UK

<sup>5</sup> Department of Physics and Astronomy, University of Waterloo, Waterloo, ON N2L 3G1, Canada

<sup>6</sup> Waterloo Centre for Astrophysics, University of Waterloo, Waterloo, ON N2L 3G1, Canada

<sup>7</sup> Department of Physics and Astronomy, Haverford College, 370 Lancaster Avenue, Haverford, PA 19041, USA

<sup>8</sup> Cardiff Hub for Astrophysics Research & Technology, School of Physics & Astronomy, Cardiff University, Queens Buildings, The Parade, Cardiff, CF24 3AA, UK

<sup>9</sup> Department of Physics and Astronomy, University of Victoria, Victoria, British Columbia V8P 1A1, Canada

<sup>10</sup> Department of Astronomy, University of Illinois, 1002 West Green Street, Urbana, IL 61801, USA

<sup>11</sup> Kavli Institute for Cosmology, University of Cambridge, Madingley Road, Cambridge, CB3 0HA, UK

<sup>12</sup> Cavendish Laboratory—Astrophysics Group, University of Cambridge, 19 JJ Thompson Avenue, Cambridge, CB3 0HE, UK

<sup>13</sup> Department of Physics, Florida International University, 11200 SW 8th Street, Miami, FL 33199, USA

<sup>14</sup> Department of Physics, The College of New Jersey, Ewing, NJ 08618, USA

<sup>15</sup> Institute of Astronomy and Astrophysics, Academia Sinica, No. 1, Section 4, Roosevelt Road, Taipei 10617, Taiwan

<sup>16</sup> Department of Physics & Astronomy, City University of New York, College of Staten Island, 2800 Victory Boulevard, Staten Island, NY 10314, USA

<sup>17</sup> Department of Astrophysics & Hayden Planetarium, American Museum of Natural History, Central Park West at 79th Street, New York, NY 10024, USA

<sup>18</sup> Physics Program, The Graduate Center, CUNY, New York, NY 10016, USA

<sup>19</sup> University of Alabama, Department of Physics and Astronomy, Tuscaloosa, AL 35487, USA

<sup>20</sup> Department of Physics, Tamkang University, No. 151, Yingzuan Road, Tamsui District, New Taipei City 251301, Taiwan

<sup>21</sup> Departamento de Física, CCNE, Universidade Federal de Santa Maria, Santa Maria, RS 97105-900, Brazil

<sup>22</sup> Laboratório Interinstitucional de e-Astronomia—LIneA, Rua General José Cristino 77, Rio de Janeiro, RJ—20921-400, Brazil

<sup>23</sup> Department of Physics & Astronomy, Oberlin College, Oberlin, OH 44074, USA

<sup>24</sup> Astronomy Department, University of Washington, Seattle, WA 98195, USA

<sup>25</sup> Department of Astronomy, University of Massachusetts, Amherst, MA 01003, USA

<sup>26</sup> Cosmic Dawn Center (DAWN), Jagtvej 128, DK-2200 Copenhagen N, Denmark

<sup>27</sup> Niels Bohr Institute, University of Copenhagen, Jagtvej 128, København N, DK-2200, Denmark

Received 2022 August 26; revised 2022 October 19; accepted 2022 October 21; published 2022 December 14

## Abstract

Post-starburst (PSB) galaxies have recently and rapidly quenched their star formation; thus, they are an important way to understand how galaxies transition from star-forming late types to quiescent early types. The recent discovery of large cold gas reservoirs in PSB galaxies calls into question the theory that galaxies must lose their gas to become quiescent. Optical Integral Field Spectroscopy (IFS) surveys have revealed two classes of PSB galaxies: central PSB (cPSB) galaxies with central quenching regions and ring PSB (rPSB) galaxies with quenching in their outskirts. We analyze a sample of 13 nearby ( $z < 0.1$ ) PSB galaxies with spatially resolved optical IFS data from the Mapping Nearby Galaxies at Apache Point Observatory survey and matched resolution Atacama Large Millimeter/submillimeter Array observations of  $^{12}\text{CO}(1-0)$ . Disturbed stellar kinematics in 7/13 of our PSB galaxies and centrally concentrated molecular gas is consistent with a recent merger for most of our sample. In galaxies without merger evidence, alternate processes may funnel gas inward and suppress star formation, which may include outflows, stellar bars, and minor mergers or interactions. The star formation efficiencies of the PSB regions in nearly half our galaxies are suppressed while the gas fractions are consistent with star-forming galaxies. Active galactic nucleus (AGN) feedback may drive this stabilization, and we observe AGN-consistent emission in the centers of 5/13 galaxies. Finally, our cPSB and rPSB galaxies have similar properties except the ionized and molecular gas in cPSB galaxies is more disturbed. Overall, the molecular gas in our PSB galaxies tends to be compact and highly disturbed, resulting in concentrated gas reservoirs unable to form stars efficiently.

*Unified Astronomy Thesaurus concepts:* Post-starburst galaxies (2176); Galaxies (573); Molecular gas (1073); Galaxy quenching (2040); Galaxy evolution (594)

## 1. Introduction

The global star formation rates (SFRs) of galaxies form a bimodal distribution, resulting in a division between star-forming late-type galaxies (LTGs) and quiescent early-type galaxies (ETGs; Kauffmann et al. 2003b). A galactic color–



magnitude diagram quantifies this divide with primarily ETGs occupying the red sequence and LTGs dominating the blue cloud (Baldry et al. 2004; Jin et al. 2014). Blue cloud galaxies are generally star forming, gas-rich, and have disk morphologies, whereas red sequence galaxies are predominantly quiescent and gas-poor (Blanton & Moustakas 2009).

A significant population of galaxies has transitioned from the blue cloud to the red sequence over the last  $\sim 6$  Gyr (Bell et al. 2007, 2012; Ilbert et al. 2013). Galaxies undergoing such a transition must somehow quench their star formation and eventually deplete their gas reservoirs. While many quenching and gas expulsion mechanisms have been proposed, there is much work remaining to fully understand the relative importance of these processes through cosmic time.

A successful quenching mechanism must either deplete the galaxy’s gas reservoirs or suppress star formation by making it more difficult for the gas to collapse and form stars. Galaxies could lose their molecular gas by expelling their gas through outflows (e.g., Feruglio et al. 2010; Baron et al. 2017), exhausting their gas reservoirs in a starburst or from a lack of gas accretion (Bekki et al. 2002; Davis et al. 2011), and finally through environmental processes such as ram pressure stripping (Gunn & Gott 1972; Chung et al. 2009) or fast galaxy interactions (Mihos 1995; Moore et al. 1996; Bekki 1998). While these mechanisms may be important in removing gas from galaxies as they transition to the red sequence, the existence of quenched and quenching galaxies with significant molecular gas reservoirs demonstrates that quenching mechanisms that stabilize the molecular gas against star formation are also important. These processes suppressing star formation could include active galactic nuclei (AGNs) and stellar feedback (e.g., Heckman et al. 1990; Kaviraj et al. 2007; Cicone et al. 2014), morphological quenching (Martig et al. 2009), and stellar bars (Salim et al. 2020).

The ability of the gas to collapse and form stars can be captured by the star formation efficiency (SFE) of a galaxy, the SFR per molecular gas mass. On a cloud scale, the SFE is governed by sub-kiloparsec gas properties such as turbulence (Krumholz & McKee 2005; Murray 2011; Federrath & Klessen 2012; Krumholz et al. 2012), whereas global star formation properties of galaxies are impacted by global galaxy properties and the galaxy’s environment (Bluck et al. 2020). Thus, to fully understand the evolution of gas and star formation in a galaxy, both global and local scales must be considered.

To gain a better understanding of how various quenching mechanisms transform star-forming galaxies to quiescent ones, we study the population of galaxies currently undergoing this transition. Schawinski et al. (2014) found that optically green colors alone are not enough to classify a transitioning population, as many late-type green valley (GV) galaxies are typical spiral galaxies with a larger buildup of intermediate-age stars or an excess of dust. Post-starburst (PSB) galaxies are ideal for studying short-timescale evolution to quiescence as they have recently (in the last gigayear) and rapidly quenched their star formation.

Classical PSB galaxies, or “E/K+A” galaxies, are galaxies with a dominant intermediate-age (A-star) stellar population and a lack of emission lines typically associated with star formation, such as  $H\alpha$  or  $[O\text{II}]\lambda 3727\text{ \AA}$ . These characteristics indicate a recent, rapid quenching of star formation after a starburst, leaving a dominant A-type stellar population

(typically identified with Balmer series absorption lines) and little-to-no ongoing star formation. Though classical PSB galaxies have indeed quenched their star formation recently, they represent an older population of transitioning galaxies as the strict cut on emission line strength removes PSB galaxies at the beginning of their transition. Emission line cuts can select against PSB galaxies hosting energetic processes that produce emission lines, such as shocks and AGN, though more recent E+A selection methods allow for lines associated with these processes such as  $[N\text{II}]$  (e.g., Wild et al. 2007; Greene et al. 2021). Other PSB galaxy selection methods require emission line ratios consistent with shock excitation (Alatalo et al. 2016b), or have no emission line requirements at all (Wild et al. 2007, 2009; Rowlands et al. 2015, 2018). Different PSB galaxy selection methods result in overlapping but distinct samples with different physical properties. A detailed discussion of PSB galaxy selection criteria can be found in French (2021).

Recently, a number of studies have begun to probe the conditions of the interstellar medium (ISM) in PSB galaxies, yielding insights into the mechanisms driving star formation suppression in these galaxies. Crucially, these studies find that PSB galaxies have significant molecular gas reservoirs (French et al. 2015; Rowlands et al. 2015; Alatalo et al. 2016a) and dust content (Alatalo et al. 2017; Smercina et al. 2018; Li et al. 2019) despite their lack of ongoing star formation. Thus, gas removal or exhaustion is not necessary for star formation suppression in PSB galaxies, but the unresolved nature of most of these studies makes it difficult to determine why the gas is not forming stars.

The optical integral field unit (IFU) survey Mapping Nearby Galaxies at Apache Point Observatory (MaNGA) has revealed spatially resolved PSB regions within galaxies (Chen et al. 2019; Greene et al. 2021). Chen et al. (2019) differentiate between central PSB (cPSB) and ring PSB (rPSB) galaxies, depending on where the PSB regions reside. cPSB galaxies include galaxies with central regions dominated by PSB signatures and show evidence of a recent disruptive event such as a major merger, likely leading to global quenching. rPSB galaxies show PSB signatures on the outskirts of the galaxy—though not necessarily forming a full *ring*, with star formation ongoing in the center, potentially due to a disruption of gas fueling to the outer regions. Chen et al. (2019) show that cPSB and rPSB galaxies have different kinematic properties and star formation histories (SFHs), indicating that these two types of PSB galaxies have distinct origins and are not sequential evolutionary phases. Further, the overall evolution of rPSB galaxies is uncertain as it is unclear whether an rPSB galaxy phase leads to global galaxy quenching or if this is a temporary phase and star formation is re-invigorated in the outskirts.

We analyze a sample of 13 nearby ( $z < 0.1$ ) PSB galaxies with MaNGA and Atacama Large Millimeter/submillimeter Array (ALMA) data to characterize the molecular gas and star formation properties on kiloparsec scales in PSB galaxies. We adopt a flat Lambda cold dark matter cosmology with  $H_0 = 70\text{ km s}^{-1}\text{ Mpc}^{-1}$ ,  $\Omega_m = 0.30$ , and  $\Omega_\Lambda = 0.70$ . This paper is organized as follows. Section 2 presents the MaNGA and ALMA data and our sample of PSB galaxies. Section 3 describes our methods of computing molecular gas masses from the ALMA data and the spectral fitting of the MaNGA IFU data to obtain galaxy properties such as SFRs. We present

our results in Section 4 and discuss the implications of our results in Section 5.

## 2. Observations and Sample

### 2.1. The MaNGA Survey

The MaNGA survey (Bundy et al. 2014) consists of optical IFU observations for 10,000 galaxies with  $0.01 < z < 0.15$ , taken with the Baryon Oscillation Spectroscopic Survey spectrograph (Smee et al. 2013; Drory et al. 2015) on the 2.5 m Sloan Digital Sky Survey (SDSS) telescope (Gunn et al. 2006) as one of three major SDSS-IV programs (Blanton et al. 2017). Each galaxy is covered by 19–127 hexagonal fiber bundles, covering a  $12''$ – $32''$  diameter on the sky. The resulting data cubes have a point-spread function with an FWHM of  $\sim 2''$ , and have wavelength coverage from 3600–10300 Å with  $R \sim 2000$ . MaNGA observations are calibrated with standard stars observed simultaneously, with an absolute calibration of better than 5% for  $\sim 90\%$  of the wavelength range (Yan et al. 2015). Two-thirds of MaNGA galaxies belong to the primary sample with fields of view covering 1.5 times the effective radius ( $R_e$ ), while the remaining third, the secondary sample, has coverage out to  $2.5 R_e$ . Both samples are selected with a flat stellar mass distribution and have mean physical resolutions of 1.37 and 2.5 kpc for the primary and secondary samples, respectively. More information on the MaNGA observing strategy, calibration, and survey design can be found in Law et al. (2015), Yan et al. (2015), and Wake et al. (2017).

Throughout this work, we use MaNGA emission line properties and stellar velocities from the MaNGA Data Analysis Pipeline (DAP; Belfiore et al. 2019; Westfall et al. 2019), accessed through Marvin (Cherinka et al. 2019).

### 2.2. Sample Selection

We first selected PSB galaxies from the MaNGA survey in the SDSS data release 15 (DR15), including approximately half of the galaxies in the completed survey of 10,000 galaxies (Aguado et al. 2019). We started with the 68 galaxies in the cPSB and rPSB galaxy samples of Chen et al. (2019) (excluding the irregular PSB galaxies) with additional PSB galaxies from the principal component analysis (PCA) selection method of Rowlands et al. (2018), adding another 25 galaxies, for a total of 93 galaxies. Chen et al. (2019) select PSB spaxels with  $H\delta_A > 3 \text{ \AA}$ ,  $W(H\alpha) < 10 \text{ \AA}$ , and  $\log W(H\alpha) < 0.23 \times H\delta_A - 0.46$ , where  $H\delta_A$  is the Lick index measuring the amount of  $H\delta$  absorption and  $W(H\alpha)$  is the equivalent width of  $H\alpha$  in emission.

PSB galaxies are selected with the PCA method by requiring that the central  $0.5R_e$  (the  $r$ -band half-light radius) is visually dominated by PSB spaxels. This threshold was chosen to capture PSB galaxies selected with other methods, such as the central  $3''$  fiber from SDSS Data Release 7 in Wild et al. (2007), or spatially resolved studies like that of Chen et al. (2019). With this criterion, we find that 44/4706 DR15 galaxies are PSB galaxies, similar to the 1%–3% prevalence of PSB galaxies in the local universe (e.g., Goto et al. 2003; Rowlands et al. 2018). The *eigenspectra*, or principal components, are from Wild et al. (2007), and were generated from model galaxies with star formation histories containing starbursts of various burst mass fractions, durations, and burst times, with simple stellar population templates from Bruzual & Charlot (2003). The first principal component (PC1)

corresponds to the 4000 Å break strength (the  $D_n4000$  index), and the second (PC2) is the excess Balmer absorption over what is expected given the 4000 Å break strength. The MaNGA spectrum for each spaxel with stellar velocity uncertainty  $< 500 \text{ km s}^{-1}$  is shifted to the rest frame and projected onto the model-derived principal components to determine the contribution of each. PSB spaxels are identified primarily by their strong Balmer absorption (PC2), as in Rowlands et al. (2018). After the sample selection, we slightly alter the classification boundaries, which we discuss in more detail in Appendix A.

Of the 93 PSB galaxies from the combined Chen et al. (2019) sample and PCA sample, 23 have decl.  $< 27^\circ$  and are thus observable by ALMA. To estimate the required sensitivity for our CO(1–0) ALMA observations, we used the integrated fluxes from single-dish CO(1–0) observations when available. Otherwise, we estimated the gas fraction and molecular gas mass of each galaxy with the mid-infrared Wide-field Infrared Survey Explorer (WISE) colors following Yesuf et al. (2017), or conservatively assumed a gas fraction of 3% when WISE data are not available. We selected 3% as this is a reasonable constraining limit on the gas fraction for PSB galaxies (e.g., French et al. 2018). To limit the integration time, we selected 13 galaxies with required sensitivities  $> 4 \text{ mJy beam}^{-1}$  for a  $5\sigma$  CO(1–0) detection and without previous CO observations of similar kiloparsec-scale resolution.

Our spectral fitting results (discussed in Section 3.2) reveal that one galaxy we observe with ALMA, 8939-3703, is a star-forming interloper, despite deep Balmer absorption. We therefore do not consider this galaxy in our main analysis, though we present the ALMA and MaNGA data for this galaxy in Appendix B.

One rPSB galaxy in MaNGA, 8955-3701, has similar ALMA CO(1–0) observations as part of the ALMA-MaNGA QUenching and STar-formation (ALMaQUEST) survey<sup>28</sup> (Lin et al. 2020). We include this galaxy in our final sample for a total of 13 galaxies with nine cPSB galaxies and four rPSB galaxies.

Two galaxies in our final sample are not in the Chen et al. (2019) sample and are selected from the PCA method, 8086-3704, 9088-9102, and the star-forming interloper 8939-3703. A key advantage of the PCA selection is that PC2 includes the excess absorption of all Balmer lines simultaneously, and thus can be applied to spaxels of a much lower signal-to-noise ratio (S/N) than traditional Balmer absorption measurements, such as  $H\delta$  absorption. Additionally, emission lines are masked, so our sample does not exclude PSB galaxies with emission lines excited by AGN (Yan et al. 2006, 2009; Wild et al. 2007), shocks (Alatalo et al. 2016b), and younger PSBs that have not totally ceased star formation.

Figure 1 shows the SDSS 3-color image, the PCA spaxel classification maps, and excess Balmer absorption for each galaxy in our sample. We compare our spaxel classification maps to the ring and central PSB classifications made by Chen et al. (2019), and find consistent determinations by visual inspection with the exception of 8080-3704 and 9194-3702, where the PCA classification shows a cPSB morphology, but they are classified as rPSB galaxies in Chen et al. (2019). We classify these galaxies as cPSB galaxies for the remainder of our analysis for consistency with our PCA classification maps. Additionally, 8982-6104 is an rPSB but the PCA classification

<sup>28</sup> [arc.phys.utoronto.ca/~almaquest/](http://arc.phys.utoronto.ca/~almaquest/)

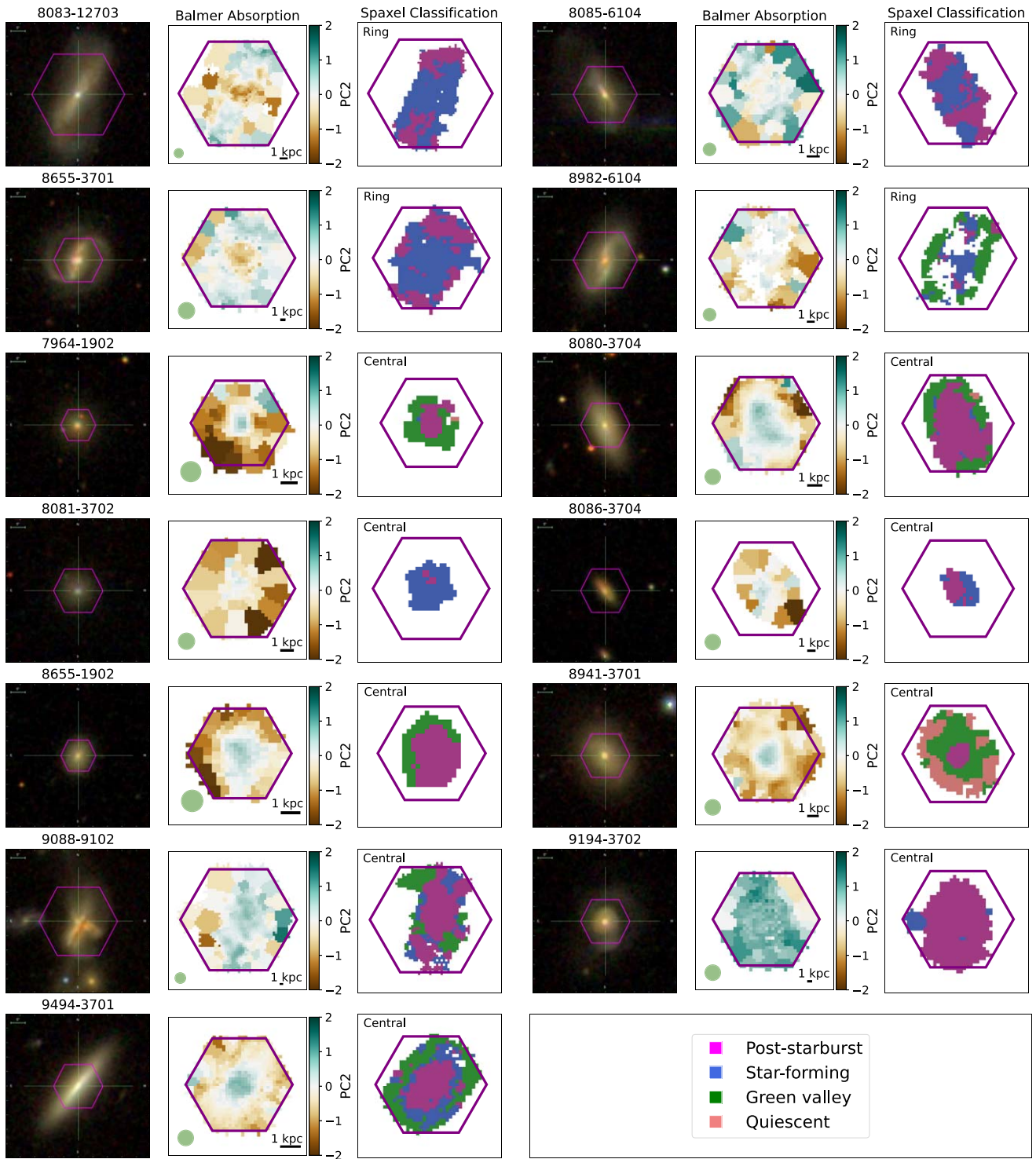


**Figure 1.** PCA classification results for our sample. Three images show the SDSS 3-color image for each galaxy, the excess Balmer absorption (PC2), and the PCA classification map. The MaNGA Plate-IFU number is above the first panel. The excess Balmer absorption is measured with the PCA method from Rowlands et al. (2018), where positive values (in teal) indicate PSB regions. The length of the black rectangle in the lower right shows the spatial scale of 1 kpc. The green ellipse in the bottom left shows the  $2''/5$  MaNGA average seeing. Finally, in the PCA classification map, PSB spaxels are magenta, SF spaxels are blue, GV spaxels are green, and quiescent spaxels are light red. The top-left text states whether the galaxy is classified as a cPSB or rPSB galaxy. The purple hexagons show the MaNGA IFU coverage.

was unable to accurately decompose the spectra of a number of central spaxels, potentially due to AGN contamination, or a strong starburst. However, we still identify this as an rPSB galaxy, even though the ring quenching region is patchy. We stress that there are a plethora of different PSB galaxy selection

criteria, and no single selection will include all spectra considered PSB galaxies (French 2021).

We plot the stellar mass versus redshift and color–magnitude diagram of our final sample of 13 galaxies and the parent MaNGA DR15 sample in contours in Figure 2. Magnitudes and

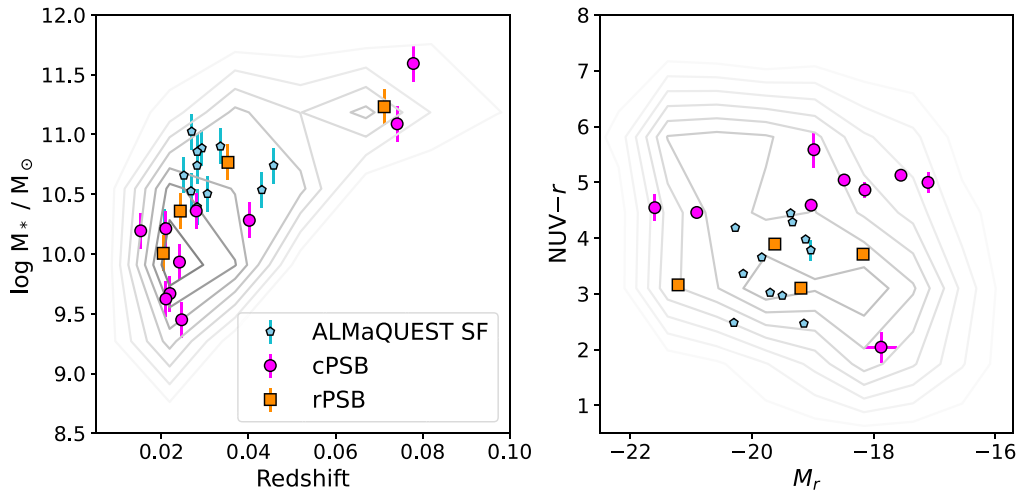


**Figure 2.** Left: stellar mass and redshift diagram of our sample of cPSB and rPSB galaxies, ALMaQUEST star-forming galaxies, and the parent MaNGA DR15 sample as gray contours. We use stellar masses from Pace et al. (2019), and see that the majority of our PSB sample has lower masses than the ALMaQUEST star-forming sample. Right: color–magnitude diagram with the same galaxies plotted. Magnitudes are from the NSA. Error bars are present for all points but may be smaller than the marker size. Our cPSB galaxies tend to be redder than the star-forming sample while our rPSB galaxies have similar colors.

redshifts are obtained from the NASA-Sloan Atlas<sup>29</sup> (NSA), and stellar masses from Pace et al. (2019) with a color mass-to-light relation aperture correction. We use an uncertainty of 0.15 dex for the integrated stellar masses based on uncertainty estimates from Pace et al. (2019). We also plot the star-forming *main-sequence* sample of 12 galaxies from ALMaQUEST, which have a specific star formation rate (sSFR)  $> 10^{-10.5} \text{ yr}^{-1}$  (Lin et al. 2022). The main-sequence sample (hereafter, star forming) also excludes the 12 ALMaQUEST galaxies selected specifically for their starburst properties in Ellison et al. (2020), making up the ALMaQUEST starburst sample. The remaining 22 ALMaQUEST galaxies constitute the GV sample with low sSFRs indicating ongoing quenching. The main-sequence galaxies are a convenient comparison sample for our PSB galaxies because of their similar ALMA observations, though we emphasize that the majority of our sample has significantly lower stellar masses.

We also note that the spectral-fitted stellar masses from Pace et al. (2019) for our PSB galaxies are not fully reliable due to the unique and complex SFHs of PSB galaxies. Hence, we include these total stellar masses not as precise values but as a rough estimate for our sample.

In the color–magnitude diagram shown in Figure 2, our cPSB galaxies tend to be redder than the ALMaQUEST star-forming galaxies as we expect for a globally quenching population. Our rPSB galaxies have comparable colors to the star-forming galaxies, as is consistent with their actively star-forming centers.

### 2.3. ALMA Observations

We obtain ALMA 12 m array band 3 observations for 13 galaxies (12 PSB galaxies and one interloper) in ALMA proposal 2019.1.01136.S (P.I. Rowlands), listed in Table 1. Each observation has four 1.875 GHz wide spectral windows, one covering the redshifted  $^{12}\text{CO}(1-0)$  line with a rest frequency of 115.27 GHz, and the other three covering nearby redshifted  $\text{CH}_3\text{OH}$ ,  $\text{CN}$ , and  $\text{HC}_3\text{N}$  lines with rest frequencies of 107.02, 113.5, and 100.07 GHz, respectively. These

observations have minimum baselines of 15 m and a maximum of 314 m (corresponding to configuration C-2) with the exception of 9088-9102, which had a maximum baseline of 440 m. Integration times range from 300–6400 s. The native velocity resolution is  $3 \text{ km s}^{-1}$  and the native angular resolutions range from  $2''.5$ – $3''$ .

The observations were pipeline calibrated and imaged with the Common Astronomy Software Applications package (CASA v6.4.3, McMullin et al. 2007). We construct data cubes from each spectral window and image the continuum with the `tclean` task. In each case, we use a circular clean mask centered on the middle of the image (approximately coincident with the optical center of each galaxy) and with a radius extending slightly beyond the extent of the CO emission. Following the ALMaQUEST survey (Lin et al. 2020), we use a circular restoring beam with an FWHM of  $2''.5$  and specify the pixel size of our millimeter data as  $0''.5$  to match the seeing and pixel scale of the MaNGA data for an optimal comparison between the ALMA and MaNGA data. We use Briggs weighting with a robust parameter of 0.5 and a flux threshold of the  $1\sigma$  noise level for all data products except the non-CO spectral windows where we use a robust parameter of 2 to maximize sensitivity.

We image the continuum using all four of the spectral windows, flagging out channels from the CO spectral window within  $1000 \text{ km s}^{-1}$  of the redshifted  $\text{CO}(1-0)$  frequency. We include the entirety of the non-CO spectral windows because we do not detect any non-CO line emission.

We apply continuum subtraction to the galaxies with continuum detections with the CASA task `uvcontsub`. We image the CO spectral windows with a spectral channel width of  $11 \text{ km s}^{-1}$ . For direct comparison between the CO and MaNGA data, we employ the `imregrid` task in CASA to match the pixel locations in both images.

We generate integrated  $\text{CO}(1-0)$  intensity, velocity, and velocity dispersion maps for each galaxy (the moment 0, 1, and 2 maps, respectively). We set the velocity bounds of the moment maps based on the width of the  $\text{CO}(1-0)$  line in the total spectrum within  $1.5 R_e$  of each galaxy, as shown in Figure 3. We use the  $r$ -band half-light radius from the NSA as  $R_e$  throughout this work. For the integrated intensity, we do not

<sup>29</sup> <http://nsatlas.org/>

**Table 1**  
Observations for Each Target from ALMA Proposal 2019.1.01136.S

MaNGA Plate-IFU (1)	Observation Time (s) (2)	Observation Date (3)	Line Sensitivity (mJy beam <sup>-1</sup> ) (4)	Native Beam Size ( $\theta_{\text{maj}}'' \times \theta_{\text{min}}''$ ) (5)
7964-1902	695.5	2019 Nov 24	0.9	2''8 × 2''3
8080-3704	302.4	2019 Dec 23	1.1	3''1 × 2''5
8081-3702	5745.6	2019 Dec 25	0.3	2''9 × 2''3
8083-12703	302.4	2019 Dec 14	0.7	2''9 × 2''2
8085-6104	302.4	2019 Dec 14	1.5	2''8 × 2''3
8086-3704*	302.4	2019 Dec 14	1.1	2''7 × 2''4
8655-1902	302.4	2019 Dec 13	1.7	3''1 × 2''4
8939-3703*	635.0	2019 Dec 31	0.9	3''5 × 2''4
8941-3701	1844.6	2019 Dec 14	0.7	3''3 × 2''4
8982-6104	302.4	2019 Nov 23	1.2	3''5 × 2''5
9088-9102*	6531.8	2020 Jan 2	0.4	2''6 × 2''5
9194-3702	302.4	2019 Dec 24	0.9	3''0 × 2''5
9494-3701	3870.7	2020 Jan 1	0.6	2''9 × 2''4

**Note.** (1) MaNGA Plate-IFU identifier. Galaxies marked with \* were selected with the PCA method and are not in the Chen et al. (2019) sample. (2) Integration time of ALMA observation. (3) Date of ALMA observation. (4) Computed CO line sensitivity. The line sensitivity is calculated from a line-free region of each data cube. (5) The native beam size of the observations.

apply any sigma clipping, while we remove pixels less than the  $4\sigma$  noise level for the velocity and velocity dispersion maps.

We image the remaining three continua-subtracted spectral windows, centered on the CH<sub>3</sub>OH, CN, and HC<sub>3</sub>N lines, with a Briggs robust parameter of 2 in order to maximize the sensitivity of our data, and a similar flux threshold of  $1\sigma$  and spectral channel width of  $11 \text{ km s}^{-1}$ , using the native beam size. We do not detect these emission lines in any of our galaxies.

Both the imaging and moment map creation follow the methods of the ALMaQUEST survey (Lin et al. 2020), including the use of the MaNGA beam size, allowing for a robust comparison of our sample with their similar observations of star-forming and GV galaxies. As mentioned in Section 2.2, we include one rPSB galaxy from the ALMaQUEST survey in our sample, 8655-3701. The data for this galaxy is slightly different from the rest of our sample with a lower spectral resolution CO spectral window and a single dedicated continuum spectral window. We image the continuum as above, though with only the single continuum spectral window and the channels of the CO spectral window at least  $1000 \text{ km s}^{-1}$  away from the expected CO line frequency. We image the CO spectral window in an identical way to the rest of our sample, as our chosen channel width of  $11 \text{ km s}^{-1}$  is equivalent to the spectral resolution of this data. We do not have spectral coverage of the CH<sub>3</sub>OH, CN, and HC<sub>3</sub>N lines for this galaxy.

As shown in Table 1, the native beam sizes of our observations tend to be slightly higher than the MaNGA seeing of 2''.5. To ensure that our choice of a smaller restoring beam does not impact our results, we image our data products with the native beam size and find similar results with no systematic offsets. The data cubes with the selected 2''.5 restoring beam tend to have slightly higher noise levels than in the data cubes imaged with the native restoring beam, up to  $\sim 10\%$  for the cubes with the largest native beam sizes. For consistency, we use the 2''.5 restoring beam fluxes and noise maps, which may yield a slight overestimate of our uncertainties.

### 3. Methods

#### 3.1. Molecular Gas Masses

We compute molecular gas masses from the integrated CO(1–0) intensity maps with Equation (1), following Bolatto et al. (2013) with a constant, Milky Way conversion factor of  $\alpha_{\text{CO}} = 4.35 M_{\odot} (\text{K km s}^{-1} \text{ pc}^2)^{-1}$ , including a helium correction,

$$M_{\text{H}_2} = \alpha_{\text{CO}} * L_{\text{CO}}. \quad (1)$$

The value of  $\alpha_{\text{CO}}$  represents a significant source of uncertainty, especially given that  $\alpha_{\text{CO}}$  can be as low as  $0.8 M_{\odot} (\text{K km s}^{-1} \text{ pc}^2)^{-1}$  in extreme environments such as in starburst galaxies (Narayanan et al. 2011). We discuss our results with a variable  $\alpha_{\text{CO}}$  in Appendix C.

We report the global CO and continuum properties of our sample in Table 2. More details on the continuum emission and radio detections of our sample are in Appendix F.

#### 3.2. Spectral Fitting

To obtain SFHs, we fit the optical MaNGA spectra of the PSB galaxies using BAGPIPES (Carnall et al. 2018, 2019), a fully Bayesian spectral fitting code. We stack all spaxels classified as PSB through PCA (Section 2.2) after careful removal of flagged spaxels in MaNGA suffering from foreground stars, dead fiber, or low S/N. Stacking is performed by simple unweighted summing, and uncertainties are summed in quadrature. We do not correct for the stellar or gas velocities in individual spaxels. To match the spectral sampling rate  $R \sim 2000$  of MaNGA spectra, we limit our fitted spectral range to the rest frame  $\lambda < 7500\text{\AA}$ , the limit of the stellar templates from the MILES library (Falc3n-Barroso et al. 2011).

BAGPIPES uses the 2016 version of the Bruzual & Charlot (2003) spectral synthesis models, and assumes the initial mass function from Kroupa (2001). We adopt the two-component SFH functional form from Wild et al. (2020) designed to

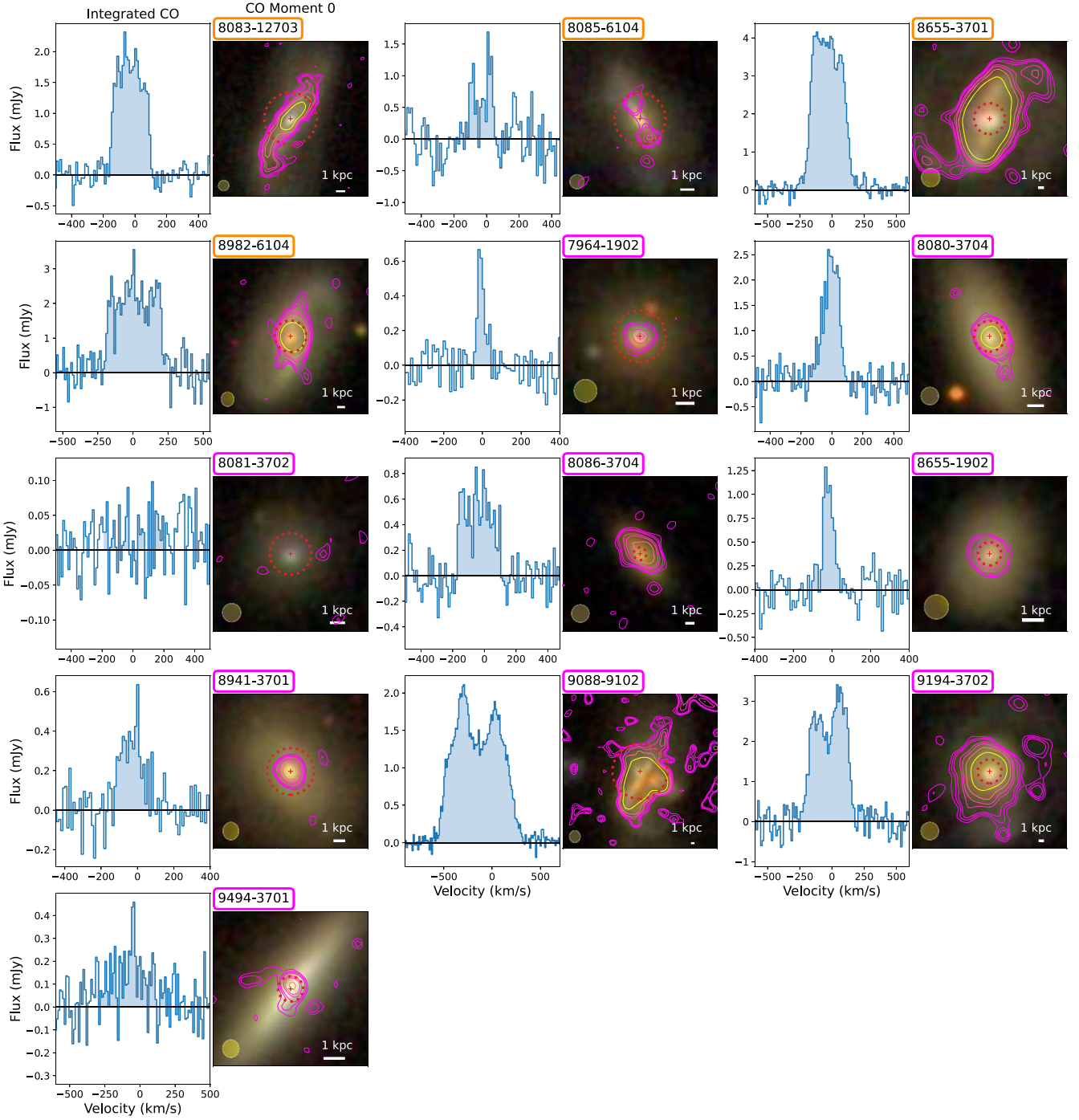


**Figure 3.** CO(1–0) spectra and integrated intensity contours for the 13 PSB galaxies in our sample. The spectra is spatially integrated over  $1.5R_e$ . The shaded region shows the spectral integration bounds for the intensity maps. The MaNGA Plate-IFU identifier is boxed in purple for cPSBs galaxies and orange for rPSB galaxies. The CO moment 0 contours correspond to S/N values of 3, 4, 5, 8, 10, 15, and 30, and are plotted over the SDSS 3-color image. The  $1\sigma$  noise levels for each galaxy are given in Table 1. The red plus denotes the optical center of the galaxy, and the red dashed line denotes the  $r$ -band effective radius from the NSA. The yellow circle in the lower left denotes the ALMA beam size.

describe PSB galaxies:

$$\text{SFR}(t) \propto \frac{1 - f_{\text{burst}}}{\int \psi_e dt} \times \psi_e(t) \Big|_{t_{\text{form}} > t > t_{\text{burst}}} + \frac{f_{\text{burst}}}{\int \psi_{\text{burst}} dt} \times \psi_{\text{burst}}(t) \quad (2)$$

where  $t_{\text{form}}$  is the lookback time when the older population began to form,  $t_{\text{burst}}$  is the time since the peak of the starburst, and  $f_{\text{burst}}$  is the portion of mass formed during the starburst.  $\psi_e$  and  $\psi_{\text{burst}}$  are given by

$$\psi_e(t) = \exp^{-\frac{t}{\tau_e}}, \quad (3)$$

**Table 2**  
Integrated CO and Continuum Properties of Our Sample

Plate-IFU	R.A.	Decl.	$z$	PSB Type	$S_{\text{CO}}$ (Jy km s <sup>-1</sup> )	$\log M_{\text{H}_2}/M_{\odot}$	CO $R_{50}$ (kpc)	$S_{3 \text{ mm}}$ (mJy)	$\sigma_{3 \text{ mm}}$ (mJy)
(1)	(2)	(3)	(4)	(5)	(6)	(7)	(8)	(9)	(10)
7964-1902	21:09:41.43	00:37:39.97	0.024	cPSB	0.8±0.2	7.99±0.08	0.7	...	...
8080-3704	03:17:49.79	-00:33:16.77	0.021	cPSB	8.4 ± 0.4	8.86 ± 0.02	0.6	0.23 ± 0.02	0.035
8081-3702	03:19:47.24	00:37:25.76	0.025	cPSB	<0.2	<7	...	...	...
8083-12703	03:19:43.04	00:33:55.72	0.024	rPSB	11.1 ± 0.2	9.113 ± 0.01	1.7	0.183 ± 0.005	0.013
8085-6104	03:26:50.14	00:11:54.92	0.020	rPSB	3.1 ± 0.5	8.41 ± 0.06	...	...	...
8086-3704	03:48:41.67	-00:39:03.60	0.040	cPSB	3.7 ± 0.2	9.08 ± 0.03	1.6	...	...
8655-1902	23:53:52.52	-00:05:55.43	0.022	cPSB	2.2 ± 0.2	8.33 ± 0.04	0.7	...	...
8655-3701	23:47:00.44	-00:26:50.59	0.071	rPSB	32.1 ± 0.2	10.518 ± 0.003	3.0	0.819 ± 0.009	0.025
8939-3703 <sup>†</sup>	08:23:37.68	25:01:12.42	0.021	...	<0.7	<8	...	...	...
8941-3701	08:00:14.30	26:41:52.85	0.028	cPSB	1.7 ± 0.1	8.41 ± 0.03	0.8	...	...
8982-6104	13:32:13.70	26:56:59.93	0.035	rPSB	24.5 ± 0.6	9.78 ± 0.01	1.2	0.53 ± 0.02	0.045
9088-9102	16:09:53.36	26:37:33.21	0.078	cPSB	29.9 ± 0.1	10.567 ± 0.002	3.9	0.318 ± 0.003	0.012
9194-3702	03:08:07.07	00:27:22.35	0.074	cPSB	24.7 ± 0.5	10.44 ± 0.008	3.0	0.16 ± 0.02	0.032
9494-3701	08:27:01.41	21:42:24.31	0.015	cPSB	1.6 ± 0.1	7.88 ± 0.03	1.1	0.245 ± 0.006	0.012

**Note.** (1) MaNGA Plate-IFU identifier. 8939-3703, the star-forming interloper, is denoted by <sup>†</sup> (see Appendix B). (2) Optical R.A. (J2000). (3) Optical decl. (J2000). (4) Optical redshift. (5) rPSB or cPSB classification. (6) Integrated CO flux. (7) Total molecular gas mass. (8) CO emission half-light radius (computed with *statmorph*). (9) 3 mm continuum flux. (10)  $1\sigma$  noise level of 3 mm emission.

$$\psi_{\text{burst}}(t) = \left[ \left( \frac{t}{t'_{\text{burst}}} \right)^{\alpha} + \left( \frac{t}{t'_{\text{burst}}} \right)^{-\beta} \right]^{-1}. \quad (4)$$

$\psi_e$  is the older, exponential decay component and  $\psi_{\text{burst}}$  is the double power-law starburst component.  $\tau_e$  is the older population's exponential decay timescale.  $\alpha$  and  $\beta$  are the declining and increasing timescales of the burst, respectively, with larger values corresponding to steeper SFH slopes.  $t'_{\text{burst}}$  is the age of the universe at the peak of the starburst. All times in the above equations are in the age of the universe (i.e.,  $t = 13.8$  Gyr is the present).

We implement a two-step metallicity evolution model, which allows for the stellar metallicity of newly formed stars before ( $Z_{\text{old}}$ ) and after the peak of the starburst ( $Z_{\text{burst}}$ ) to have independent metallicity levels as motivated by hydrodynamic simulations (H. Leung et al. 2022, in preparation). For dust attenuation, we use the two-component dust law from Wild et al. (2007) with a fixed power-law exponent of  $n = 0.7$  for the ISM and a steeper power-law exponent for stars younger than 10 Myr of  $n = 1.3$ . These young stars are more attenuated than the older ones by a factor  $\eta$  ( $=1/\mu$  in Wild et al. (2007), see Equation (3)), as they are assumed to be surrounded by their birth clouds. Nebular emission lines and residuals of skyline subtraction (drawing from the catalog of Hanuschik 2003) are masked during fitting.

We include a Gaussian process (GP) kernel as an additive model component to help account for correlated systematic errors caused by observational and calibration problems in the observed frame as well as model-data mismatch from model limitations (stellar templates, assumed SFH, etc.) in the rest frame (see Section 4.3 of Carnall et al. 2019). The kernel employed is a stochastically driven damped simple harmonic oscillator (SHOTerm), implemented through the *celerite2* python package (Foreman-Mackey et al. 2017; Foreman-Mackey 2018). The final model has 18 parameters, with 15 free to vary with priors. The parameter priors are listed in Appendix D. Sampling of the posterior surface is performed with the nested sampling algorithm MULTINEST (Feroz & Hobson 2008) and its python interface (Buchner et al. 2014).

For a detailed implementation of all elements of the model, its testing, and potential limitations, see H. Leung et al. (2022, in preparation).

Due to the recent starbursts dominating the contribution in the observed spectra as a result of their much lower mass-to-light ratio (see Figure 7 of French et al. 2018), the stellar mass formed during the older, pre-burst component can be underestimated by a small amount, which leads to a slight overestimation in burst mass fraction ( $f_{\text{burst}}$ ). However, since this affects all PSB galaxies, it is expected to have little qualitative effects on our results (discussed in H. Leung et al. 2022, in preparation).

After fitting, SFRs are measured as the average across the most recent  $10^8$  yr from the fitted SFHs.

We report the CO properties and spectral fitting results of the PSB regions for each galaxy in our sample in Table 3. All galaxies but one aforementioned interloper (8939-3703) exhibit clear histories of recent starburst and subsequent quenching from their fitted SFHs, as displayed in Appendix D.

## 4. Results

### 4.1. Molecular Gas Morphology

We consider the morphologies of the integrated CO intensity maps shown in Figure 3. Qualitatively, 6/12 of our PSB galaxies have molecular gas morphologies consisting of one central clump with little extended gas at our resolution. At least four of the PSB galaxies with extended gas appear to be tidally disturbed in the optical SDSS imaging: 8083-12703, 8655-3701, 9194-3702, and 9088-9102. The first three are visually classified as post-mergers by Thorp et al. (2019), and the latter is an ongoing merger, as can be seen in the SDSS image. 9088-9102 has many high-significance CO line detections separated from the galaxy itself, likely due to a plethora of gas in a dense environment. 9494-3701 has extended gas perpendicular to the disk of the galaxy, potentially indicative of gas expulsion or an outflow.

We fit each CO moment 0 map with a 2D Gaussian. We do not fit two galaxies: 8081-3702 lacks a robust CO detection,



**Table 3**  
CO and Spectral-fitted Properties of the PSB Spaxels in Our Sample

Plate-IFU	$S_{\text{CO,PSB}}$ (Jy km s <sup>-1</sup> )	$\log M_{\text{H}_2,\text{PSB}}$ (log $M_{\odot}$ )	$\log \text{SFR}$ (log $M_{\odot} \text{ yr}^{-1}$ )	$\log M_{*,\text{PSB}}$ (log $M_{\odot}$ )	$t_{\text{burst}}$ (Gyr)	$f_{\text{burst}}$	$F_{1 \text{ Gyr}}$	$A_{\text{PSB}}$ (kpc <sup>2</sup> )
(1)	(2)	(3)	(4)	(5)	(6)	(7)	(8)	(9)
7964-1902	0.44 ± 0.04	7.71 ± 0.04	-1.7 <sup>+0.1</sup> <sub>-0.1</sub>	9.24 <sup>+0.05</sup> <sub>-0.05</sub>	1.9 <sup>+0.3</sup> <sub>-0.2</sub>	0.6 <sup>+0.2</sup> <sub>-0.2</sub>	0.049 <sup>+0.007</sup> <sub>-0.006</sub>	2.7
8080-3704	8.0 ± 0.2	8.84 ± 0.01	-1.6 <sup>+0.4</sup> <sub>-1.0</sub>	10.06 <sup>+0.06</sup> <sub>-0.06</sub>	0.59 <sup>+0.09</sup> <sub>-0.04</sub>	0.12 <sup>+0.02</sup> <sub>-0.02</sub>	0.14 <sup>+0.02</sup> <sub>-0.02</sub>	26.0
8081-3702	<0.01	<6.0	-2.4 <sup>+0.1</sup> <sub>-0.1</sub>	7.75 <sup>+0.04</sup> <sub>-0.04</sub>	1.1 <sup>+0.1</sup> <sub>-0.09</sub>	0.6 <sup>+0.1</sup> <sub>-0.1</sub>	0.43 <sup>+0.07</sup> <sub>-0.09</sub>	0.6
8083-12703	2.43 ± 0.08	8.45 ± 0.02	-0.63 <sup>+0.08</sup> <sub>-0.09</sub>	9.50 <sup>+0.06</sup> <sub>-0.06</sub>	1.4 <sup>+0.3</sup> <sub>-0.2</sub>	0.5 <sup>+0.3</sup> <sub>-0.1</sub>	0.19 <sup>+0.02</sup> <sub>-0.02</sub>	63.0
8085-6104	1.1 ± 0.2	7.94 ± 0.08	-0.77 <sup>+0.07</sup> <sub>-0.08</sub>	9.27 <sup>+0.04</sup> <sub>-0.03</sub>	1.9 <sup>+0.3</sup> <sub>-0.3</sub>	0.7 <sup>+0.1</sup> <sub>-0.2</sub>	0.17 <sup>+0.03</sup> <sub>-0.02</sub>	23.3
8086-3704	1.67 ± 0.07	8.73 ± 0.02	-0.70 <sup>+0.06</sup> <sub>-0.07</sub>	9.71 <sup>+0.03</sup> <sub>-0.03</sub>	3.0 <sup>+0.4</sup> <sub>-0.5</sub>	0.73 <sup>+0.07</sup> <sub>-0.1</sub>	0.06 <sup>+0.01</sup> <sub>-0.01</sub>	14.3
8655-1902	2.0 ± 0.1	8.28 ± 0.03	-6 <sup>+3</sup> <sub>-10</sub>	9.35 <sup>+0.06</sup> <sub>-0.07</sub>	1.0 <sup>+0.3</sup> <sub>-0.1</sub>	0.3 <sup>+0.3</sup> <sub>-0.1</sub>	0.1 <sup>+0.1</sup> <sub>-0.06</sub>	7.8
8655-3701	3.40 ± 0.04	9.543 ± 0.005	-0.2 <sup>+0.1</sup> <sub>-0.1</sub>	10.28 <sup>+0.05</sup> <sub>-0.04</sub>	1.4 <sup>+0.2</sup> <sub>-0.1</sub>	0.4 <sup>+0.2</sup> <sub>-0.1</sub>	0.16 <sup>+0.02</sup> <sub>-0.03</sub>	140.1
8941-3701	1.02 ± 0.04	8.20 ± 0.02	-1.4 <sup>+0.1</sup> <sub>-0.1</sub>	9.67 <sup>+0.02</sup> <sub>-0.02</sub>	1.55 <sup>+0.09</sup> <sub>-0.09</sub>	0.90 <sup>+0.05</sup> <sub>-0.1</sub>	0.09 <sup>+0.02</sup> <sub>-0.02</sub>	4.8
8982-6104	0.61 ± 0.06	8.18 ± 0.04	-1.6 <sup>+0.1</sup> <sub>-0.1</sub>	9.3 <sup>+0.04</sup> <sub>-0.05</sub>	1.3 <sup>+0.2</sup> <sub>-0.2</sub>	0.3 <sup>+0.1</sup> <sub>-0.08</sub>	0.10 <sup>+0.03</sup> <sub>-0.02</sub>	10.6
9088-9102	24.59 ± 0.08	10.481 ± 0.001	-0.1 <sup>+0.2</sup> <sub>-0.2</sub>	11.33 <sup>+0.04</sup> <sub>-0.05</sub>	1.44 <sup>+0.09</sup> <sub>-0.3</sub>	0.15 <sup>+0.03</sup> <sub>-0.03</sub>	0.03 <sup>+0.01</sup> <sub>-0.01</sub>	628.4
9194-3702	22.1 ± 0.3	10.392 ± 0.005	0.77 <sup>+0.08</sup> <sub>-0.07</sub>	11.0 <sup>+0.04</sup> <sub>-0.04</sub>	0.81 <sup>+0.08</sup> <sub>-0.07</sub>	0.3 <sup>+0.08</sup> <sub>-0.05</sub>	0.31 <sup>+0.07</sup> <sub>-0.05</sub>	301.1
9494-3701	0.96 ± 0.05	7.65 ± 0.02	-3.1 <sup>+0.6</sup> <sub>-2.0</sub>	9.73 <sup>+0.02</sup> <sub>-0.02</sub>	0.67 <sup>+0.03</sup> <sub>-0.03</sub>	0.26 <sup>+0.03</sup> <sub>-0.03</sub>	0.31 <sup>+0.03</sup> <sub>-0.02</sub>	12.0

**Note.** (1) MaNGA Plate-IFU identifier. (2) CO flux in PSB spaxels. (3) Molecular gas mass in PSB spaxels. (4) Spectral-fitted SFR in PSB spaxels. (5) Stellar mass in PSB spaxels. (6) Lookback time to the peak of the starburst. (7) Fraction of stellar mass formed in the starburst. (8) Fraction of stellar mass formed in the last gigayear. (9) Inclination-corrected surface area of all PSB spaxels.

and 8085-6104 has two lobes of gas that cannot be adequately represented with a single Gaussian. Of the remaining 11 galaxies with reasonable Gaussian fits, four have major axis sizes consistent with the ALMA beam size within 20%, and 9/11 have major axis sizes consistent within 50% of the beam size. Following Smercina et al. (2022), we compute the fraction of CO flux within a central core,  $f_{\text{core}}$ , defined as  $3\sigma$  of the ALMA beam size centered on the Gaussian fit center. We find that 8/11 galaxies have core fractions greater than 50%, and the sample has a mean core fraction of 66%. These high core fractions show that the molecular gas reservoirs in our PSB galaxies are highly concentrated with unresolved centers, consistent with the results of Smercina et al. (2022), who also find high core fractions in PSB galaxies with even higher resolution CO observations. We plot the core fractions versus the physical resolutions of our galaxies in Figure 4.

We also compute the core fractions of star-forming ALMaQUEST galaxies, finding 3/12 galaxies have core fractions greater than 50%, and a mean core fraction of 38%. We compare the core fraction distributions of the ALMaQUEST star-forming galaxies and our PSB galaxies with a Kolmogorov–Smirnov test and find a  $p$ -value of  $p = 0.006$ ; thus, the distributions are significantly different.

Overall, at our kiloparsec-scale resolution, our PSB galaxies have more centrally concentrated molecular gas reservoirs than the ALMaQUEST star-forming galaxies. However, we note that the sample of star-forming galaxies tends to have higher stellar masses and larger optical sizes than our PSB galaxies (see Figure 2), leading to larger physical sizes of central gas reservoirs. Regardless, the central molecular gas reservoirs of our PSB galaxies are compact with sizes  $\lesssim 1$  kpc. To fully probe the concentration of the central reservoirs of molecular gas, sub-kiloparsec-scale resolution observations are needed.

#### 4.2. Gas and Stellar Kinematics

In Figure 5, we plot the CO, stellar, and H $\alpha$  velocity maps for each galaxy. The CO velocity map is described in Section 2, and is shown only for spaxels with CO S/N > 3. We also

require a  $g$ -band S/N > 5 per spaxel for the stellar velocity map, and H $\alpha$  S/N > 3 per spaxel for the H $\alpha$  velocity map.

We measure the position angle (PA) of each velocity map with the python code `PaFit`<sup>30</sup> from Appendix C of Krajnović et al. (2006), using the optical center of the galaxy. We only show PAs with  $3\sigma$  uncertainties less than 45°. Finally, we subtract the measured systemic velocities from each velocity field. We present the PAs for the CO, stellar, and H $\alpha$  velocity fields in Table 4. We measure the same PAs for the sample of 12 ALMaQUEST star-forming galaxies. By eye, a few of the PA fits do not appear to follow the velocity field. This may be the result of imposing a global PA on a velocity field, which has a changing PA with radius, as can be seen in the CO emission of 8083-12703.

We find that 5/12 CO-detected PSB galaxies (two of which are rPSB galaxies) have CO, stellar, and H $\alpha$  velocity fields with consistent (within 30°) PAs. Other PSB galaxies either lack significant CO or H $\alpha$  rotation (5/13, all cPSB galaxies), or have kinematic misalignments (3/12). 4/12 of our PSB galaxies lack CO rotation entirely, though this may be in part driven by the compactness of the CO detections at our resolution. We also find that the H $\alpha$  PAs do not always match the CO PAs, with only 5/8 galaxies with reliable PA measurements for both velocity fields agreeing. In contrast, all 12 of the ALMaQUEST star-forming galaxies have consistent CO, stellar, and H $\alpha$  PAs.

Visual inspection of many of the velocity fields in Figure 5 shows that a simple global PA does not capture velocity fields with radially dependent PAs or non-asymmetric motions. To better characterize the velocity fields, we use the Radon transform as implemented in Stark et al. (2018). In brief, the Radon transform is a nonparametric method of determining the PA as a function of radius. Stark et al. (2018) use an automated method to classify Radon profiles of velocity fields into five classes: constant, asymmetric, inner bend, outer bend, and both inner and outer bends. The various symmetric but nonconstant Radon profile classifications (i.e., inner bend, outer bend, and

<sup>30</sup> <https://www-astro.physics.ox.ac.uk/~cappellari/software/#pafit>

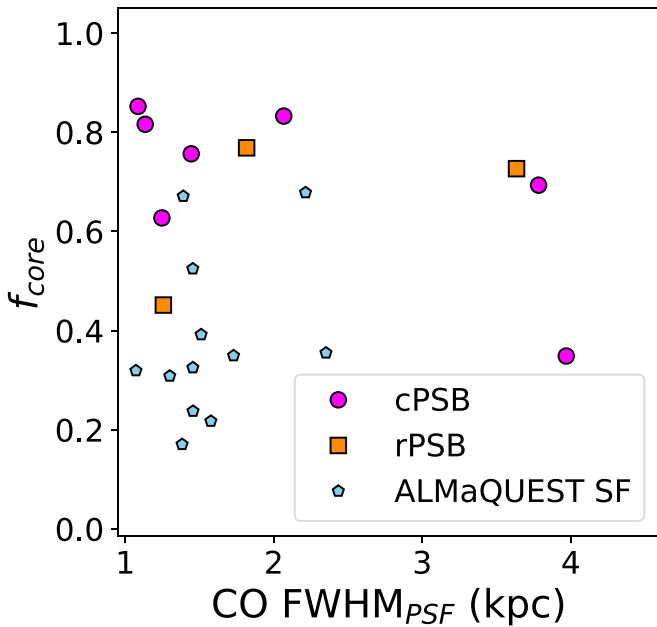


**Figure 4.** The fraction of total CO line flux within the  $3\sigma$  beam size,  $f_{\text{core}}$ , and the physical resolution of the  $2''.5$  CO beam for our cPSB galaxies in purple, rPSB galaxies in orange, and ALMaQUEST star-forming galaxies in blue. All galaxies plotted were imaged with the same  $2''.5$  circular beam. Our PSB galaxies tend to have higher core fractions and thus more centrally concentrated CO emission even at similar physical resolutions.

both inner and outer bends) appear to be driven at least in part by a combination of stellar bars, oval distortions, and disk warps, though each of these physical processes may have different Radon profile signatures. Asymmetric Radon profiles may be driven by tidal interactions due to mergers or gas infall for the  $H\alpha$  Radon profiles. We visually classify the stellar and  $H\alpha$  Radon profiles of our PSB galaxies and the ALMaQUEST star-forming galaxies, shown in Table 4. The majority of galaxies in the PSB and the ALMaQUEST star-forming samples have Radon classifications, though 1–2 galaxies in each sample cannot be classified due to a lack of rotation or spaxels with sufficient S/N. We do not compute the Radon profiles of our CO velocity fields as this method requires relatively complete velocity information over a chosen radius, such as  $R_e$ , which few of our CO velocity fields satisfy.

Our PSB galaxies are more likely to have asymmetric stellar and  $H\alpha$  Radon profiles than the ALMaQUEST star-forming galaxies. Figure 6 shows histograms of the Radon profile classifications for the stellar and  $H\alpha$  velocity fields. We combine the inner bend, outer bend, and inner bend + outer bend classifications into the symmetric bend category as our sample is too small to meaningfully split into these categories, though we emphasize different physical processes likely drive the different types of bends. For the stellar ( $H\alpha$ ) Radon profiles, 5/11 (4/11) PSB galaxies have asymmetric profiles, whereas 2/11 (1/11) are asymmetric for ALMaQUEST star-forming galaxies. While these results are suggestive, with our small sample sizes these differences are not statistically significant. From Stark et al. (2018), the percentages of asymmetric stellar and  $H\alpha$  profiles in the entire MaNGA DR15 sample are  $15.0^{+1.7}_{-1.5}\%$  and  $24.4^{+2.4}_{-2.1}\%$ , respectively. Our percentage of asymmetric stellar profiles ( $45^{+15}_{-14}\%$ ) is significantly higher than that of Stark et al. (2018) with a  $p$ -value of 0.03, whereas the percentage of asymmetric  $H\alpha$  profiles in our

sample ( $36^{+15}_{-13}\%$ ) is indistinguishable, with a  $p$ -value of 0.19. Finally, 0/4 rPSB galaxies have asymmetric  $H\alpha$  Radon profiles, while 4/8 cPSB galaxies do, but a larger sample is needed to determine if this is a physical difference.

Considering both the stellar and gas kinematics, we can classify our galaxies into three categories: those with asymmetric or nonrotating stellar velocity fields (7/13), those with symmetric stellar rotation but asymmetric or misaligned gas velocity fields (3/13), and those with consistent stellar, CO, and  $H\alpha$  rotation (3/13). In the second category, all three galaxies have constant stellar Radon profiles but either have asymmetric  $H\alpha$  Radon profiles as in 8080-3704 and 8941-3701, or are kinematically misaligned as in 9494-3701. Finally, the galaxies in the last category (8085-6104, 8086-3704, and 8982-6104) have symmetric stellar and  $H\alpha$  Radon profiles, as well as consistent CO, stellar, and  $H\alpha$  PAs. We will discuss potential physical causes for these different kinematic patterns in Section 5.

Overall, the kinematics of our PSB galaxies tend to be more complex than those of the ALMaQUEST star-forming galaxies, with misalignments and asymmetries being more common. Nearly half of our PSB galaxies (5/12) have CO,  $H\alpha$ , and stellar velocity fields rotating with a consistent PA, whereas all ALMaQUEST star-forming galaxies (12/12) have consistent PAs. Finally, we use the Radon transform to study the rotating stellar and  $H\alpha$  velocity fields and find that asymmetric Radon profiles appear to be more common in PSB galaxies than the ALMaQUEST star-forming galaxies for both stellar and  $H\alpha$  velocity fields.

### 4.3. Star Formation and Molecular Gas Properties in Context

#### 4.3.1. Global Properties

Previous single-dish CO observations of PSB galaxies have reported large molecular gas fractions despite the low SFRs of these galaxies (French et al. 2015; Rowlands et al. 2015; Alatalo et al. 2016a). In Figure 7, we plot the total molecular gas masses and the total stellar masses from Pace et al. (2019) for our sample and a number of comparison samples. In both panels, we plot the de los Reyes & Kennicutt (2019) sample of star-forming galaxies as contours. On the left, we plot the three ALMaQUEST samples: SF galaxies, GV galaxies, and SB galaxies (Lin et al. 2019, 2020; Ellison et al. 2020). On the right, we compare our PSB galaxies to unresolved CO observations of PSB galaxies, including the samples of French et al. (2015) and Rowlands et al. (2015), as well as early-type galaxies from the ATLAS<sup>3D</sup> survey (Cappellari et al. 2011; Young et al. 2011). For all the plotted samples, we use a constant  $\alpha_{\text{CO}}$  of  $4.35 M_{\odot} (\text{K km s}^{-1} \text{pc}^2)^{-1}$  for consistency. This value of  $\alpha_{\text{CO}}$  is likely an overestimate for the SB galaxies, so gas masses for this sample can be considered upper limits (Bolatto et al. 2013).

Our PSB galaxies span a range of global molecular gas fractions, from  $<1\%$  to above 20%. While some of our PSB galaxies have gas fractions similar to or greater than the majority of the de los Reyes & Kennicutt (2019) star-forming sample, four of our cPSB galaxies have low gas fractions  $\lesssim 1\%$ . Other plotted molecular gas studies of PSB galaxies similarly show a wide range of molecular gas fractions, though the greater sensitivity of our observations allows us to measure lower gas fractions down to 1%. We also see that our PSB

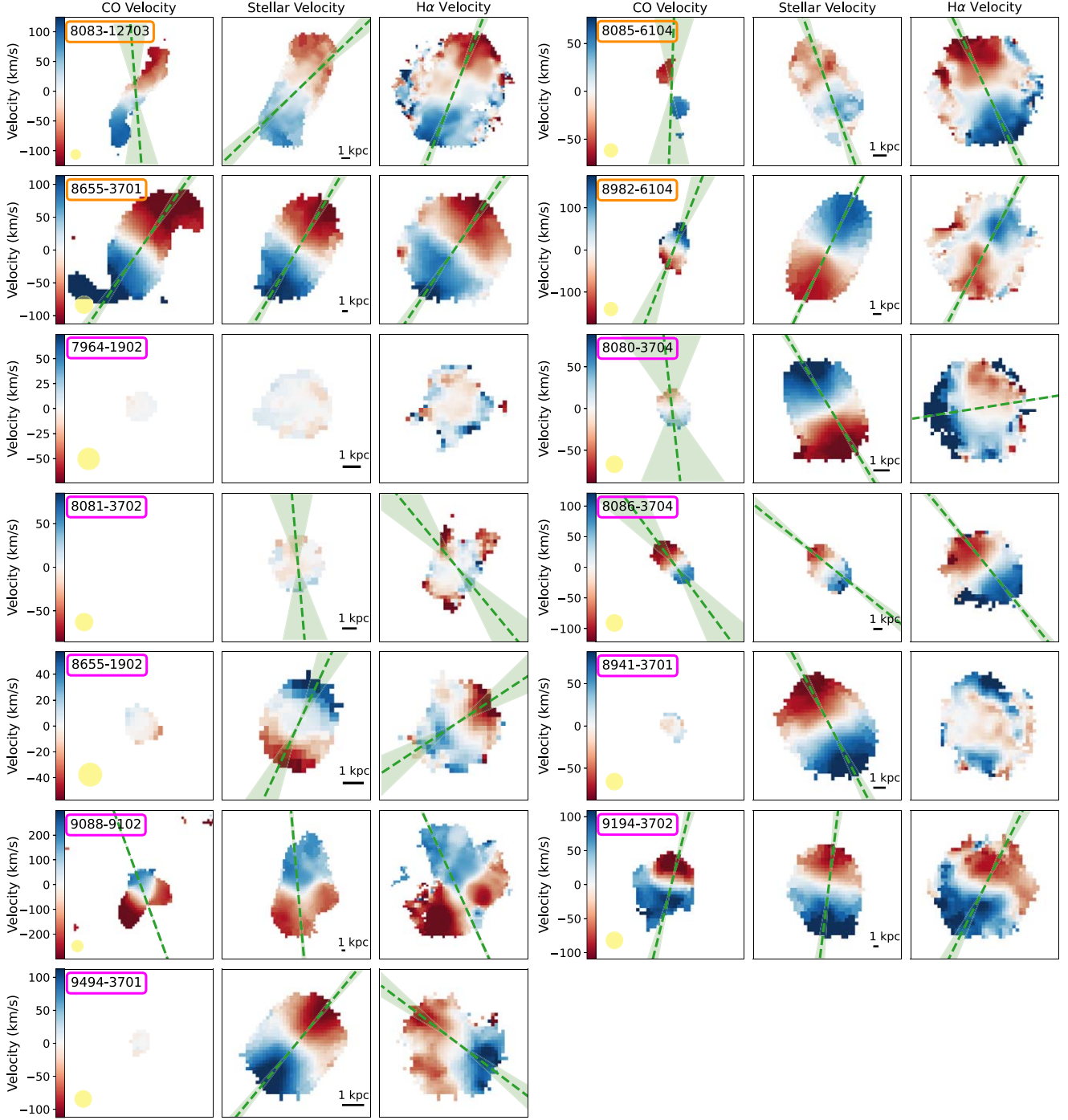


**Figure 5.** CO, stellar, and  $H\alpha$  velocity maps for each galaxy. The MaNGA Plate-IFU identifier is in the top left of the CO velocity map, boxed in magenta for cPSB galaxies and orange for rPSB galaxies. The ALMA and MaNGA beams are represented by the yellow ellipse in the bottom left. The CO velocity map is shown where we have CO S/N > 3. The stellar velocity and  $H\alpha$  maps are only shown for spaxels with an S/N of 5 or an  $H\alpha$  S/N of 3. We fit each velocity map and plot the rotational PA in green for maps with reliable PA fits, with shaded  $3\sigma$  uncertainties.

galaxies tend to have more molecular gas than the ETGs, especially for PSB galaxies with  $\log M_*/M_\odot > 10.5$ .

#### 4.3.2. PSB Regions

The link between star formation surface density and molecular gas surface density, the Kennicutt–Schmidt relation, is empirically supported in a variety of studies and physically motivated (Kennicutt 1998; de los Reyes & Kennicutt 2019). In Figure 8, we plot this relation for the PSB regions of our

galaxies compared to a variety of other studies. We only plot the properties of the PSB regions of our galaxies rather than global properties to investigate the star formation properties of the PSB regions specifically. Given that the kiloparsec-scale PSB regions have physical sizes much larger than an average giant molecular cloud for each galaxy, local small-scale variations in the molecular gas distribution will not impact our results. To compute the PSB region surface densities, we use the spectral-fitted SFR, which was measured over the entire

**Table 4**  
Kinematic Properties of Our Sample

Plate-IFU (1)	CO PA (°) (2)	Stellar PA (°) (3)	H $\alpha$ PA (°) (4)	Stellar Radon Class (5)	H $\alpha$ Radon Class (6)
7964-1902	...	...	...	A	N
8080-3704	10 $\pm$ 30	31 $\pm$ 3	99.0 $\pm$ 0.5	C	A
8081-3702	...	0 $\pm$ 20	40 $\pm$ 10	N	N
8083-12703	0 $\pm$ 10	134 $\pm$ 5	158 $\pm$ 4	A	IB
8085-6104	180 $\pm$ 20	20 $\pm$ 4	25 $\pm$ 4	IB+OB	C
8086-3704	40 $\pm$ 10	51 $\pm$ 4	39 $\pm$ 3	IB	C
8655-1902	...	160 $\pm$ 10	120 $\pm$ 10	A	C
8655-3701	146 $\pm$ 4	150 $\pm$ 4	146 $\pm$ 4	A	IB+OB
8941-3701	...	28 $\pm$ 4	...	C	A
8982-6104	158 $\pm$ 8	154 $\pm$ 2	152 $\pm$ 3	IB	IB
9088-9102	20.0 $\pm$ 0.5	5 $\pm$ 2	24 $\pm$ 1	N	A
9194-3702	166 $\pm$ 4	173 $\pm$ 4	154 $\pm$ 5	A	A
9494-3701	...	140 $\pm$ 3	53 $\pm$ 6	C	C

**Note.** (1) MaNGA Plate-IFU. (2) CO global PA. Uncertainties are  $3\sigma$  errors for all PAs. PAs are defined counterclockwise from the  $y$ -axis. (3) Stellar global PA. (4) H $\alpha$  global PA. (5) Stellar Radon profile classification. N = no classification, A = asymmetric, C = constant, IB = inner bend, OB = outer bend, IB+OB = inner bend + outer bend. (6) H $\alpha$  Radon profile classification, with the same abbreviations.

PSB region, and sum the molecular gas masses over the PSB region. We divide these by the area of the PSB regions, which we measure by multiplying the number of PSB spaxels by their inclination-corrected physical surface areas, with inclination values from the NSA. As shown in Figure 4, we are unable to resolve the central molecular gas; thus, our measured molecular gas surface densities are effectively lower limits (at least in our cPSB galaxies) as the gas could be significantly more compact than our beam size, as seen in Smercina et al. (2022) and Luo et al. (2022).

In Figure 8, we plot the SFR and molecular gas surface densities for our PSB galaxies, the star-forming sample of de los Reyes & Kennicutt (2019), and the three ALMaQUEST samples. The ALMaQUEST star formation rates are computed from the extinction-corrected H $\alpha$  emission according to Kennicutt (1998), but only for spaxels classified as star

forming according to the [S II]/H $\alpha$  versus [O III]/H $\beta$  diagram (Kewley et al. 2006). de los Reyes & Kennicutt (2019) compute SFRs for their sample with UV fluxes, correcting for dust extinction with IR fluxes. For typical star-forming galaxies, these two SFR indicators are tightly correlated (Hao et al. 2011). For the GV and SB samples, the H $\alpha$  SFRs may be underestimated in galaxies with large numbers of spaxels with AGN or composite classified spaxels, as any star formation from these spaxels is neglected.

Compared to the local star-forming galaxies in de los Reyes & Kennicutt (2019), we see that 5/13 of our PSB regions lie significantly below the fitted relation, thus having lower SFEs. In particular, 8655-1902 and 8941-3701 are two cPSB galaxies with sizable molecular gas reservoirs that have nearly quenched their star formation entirely. Other PSB regions are consistent with the Kennicutt–Schmidt relation in de los Reyes & Kennicutt (2019). Our sample is offset below the SF and SB ALMaQUEST samples with lower star formation surface densities as expected, and occupies a similar region as the GV galaxies, though often with lower gas surface densities.

In Figure 9, we plot the SFE ( $SFE = \Sigma_{SFR} / \Sigma_{M_{H_2}}$ ) and the molecular gas fraction ( $f_{H_2} = M_{H_2} / M_*$ ) of the PSB regions and the ALMaQUEST star-forming galaxies. The majority of our PSB galaxies have  $f_{H_2}$  similar to the star-forming galaxies but have suppressed SFEs, though the degree of this suppression varies significantly. One cPSB, 9494-3701, has a particularly low  $f_{H_2}$ , potentially indicating that a lack of molecular gas supply is contributing to quenching in this galaxy. We are considering the PSB regions of our galaxies rather than global properties; thus, *within* the quenching PSB region, we find that there is typically still a significant amount of gas forming stars at a suppressed rate. As discussed above, the molecular gas mass surface densities for our PSB regions are effectively lower limits, and therefore the plotted SFEs are upper limits.

#### 4.4. Molecular Gas and the SFH

Observational and theoretical studies have found a negative correlation between the post-burst age of a PSB and the molecular gas fraction (Rowlands et al. 2015; French et al. 2018; Davis et al. 2019). The timescale of the removal of molecular gas reservoirs after the starburst can provide clues about which physical mechanisms are driving this removal,

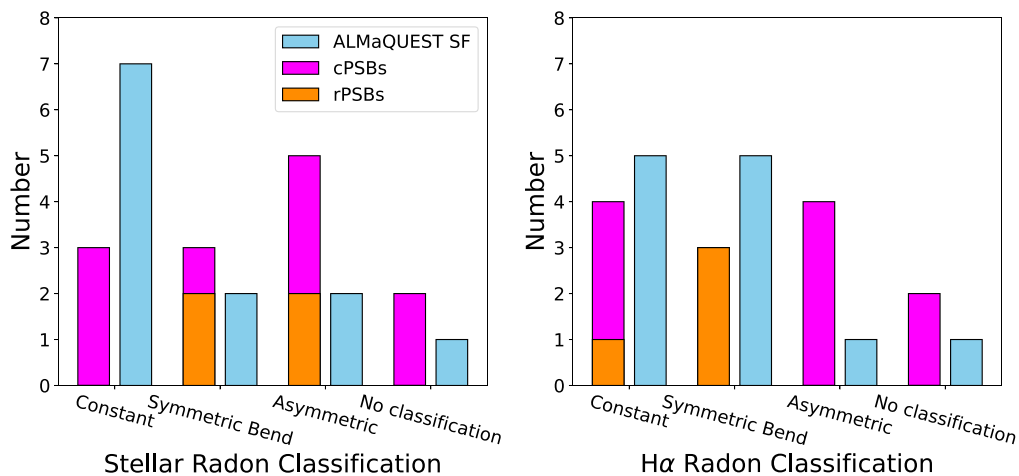


**Figure 6.** Histograms showing the Radon classifications for stellar velocity fields on the left and H $\alpha$  velocity fields on the right. cPSB galaxies are plotted in purple, rPSB galaxies in orange, and ALMaQUEST star-forming galaxies in blue. Due to our small sample, we combine the inner bend, outer bend, and inner bend + outer bend classifications from Stark et al. (2018) into the symmetric bend category. In both panels, PSB galaxies show an excess of asymmetric velocity fields.

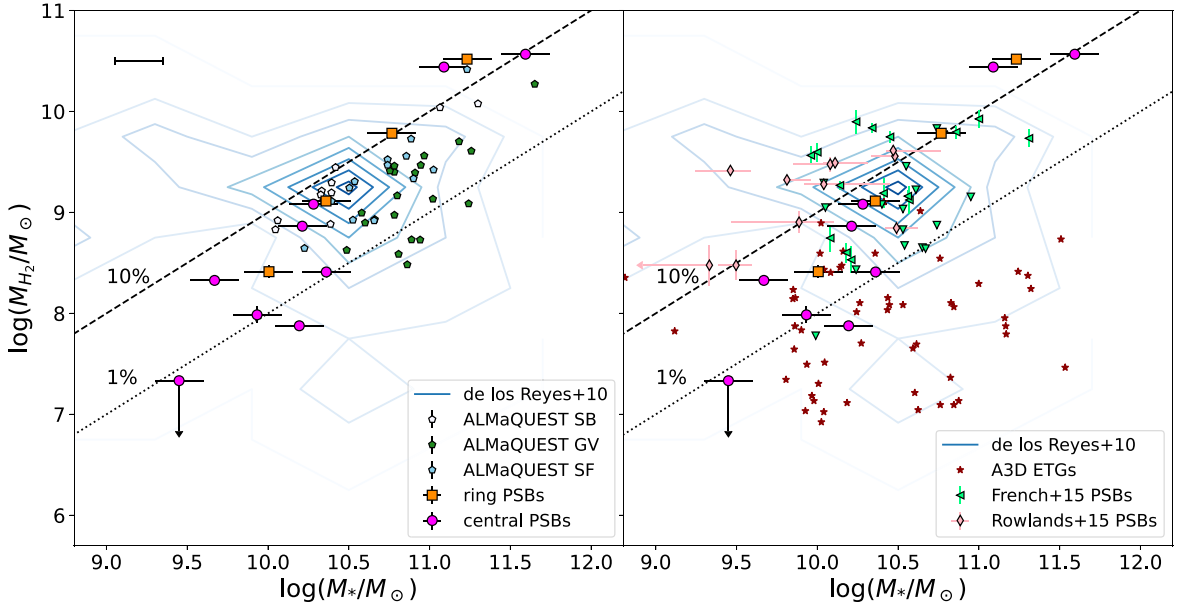


**Figure 7.** Total molecular gas and stellar masses for our cPSB galaxies and rPSB galaxies in purple and orange, respectively, with comparison samples plotted. The dotted and dashed lines show constant molecular gas fractions of 1% and 10%, respectively. The blue contours show star-forming galaxies from de los Reyes & Kennicutt (2019). In the left panel, the ALMaQUEST SF, GV, and SB samples are plotted in teal, green, and white pentagons, respectively, with molecular gas masses and SFRs summed within  $1.5 R_e$  of each galaxy. The error bar in the upper left shows typical uncertainties for the ALMaQUEST galaxies. In the right panel, two unresolved studies of PSB galaxies are shown, French et al. (2015), a sample of E+A galaxies in light green triangles, and Rowlands et al. (2015) in pink diamonds, a sample of PSB galaxies spanning a range of post-burst ages. Downward-pointing green triangles represent French et al. (2015) E+As with gas mass upper limits. ETGs from the ATLAS<sup>3D</sup> survey (Young et al. 2011) are plotted as dark red stars. We use the same  $\alpha_{\text{CO}} = 4.35 M_{\odot} (\text{K km s}^{-1} \text{pc}^2)^{-1}$  for all samples plotted. Our PSB galaxies have a wide range of molecular gas fractions; while some of our PSB galaxies are very gas-rich, others have little molecular gas.

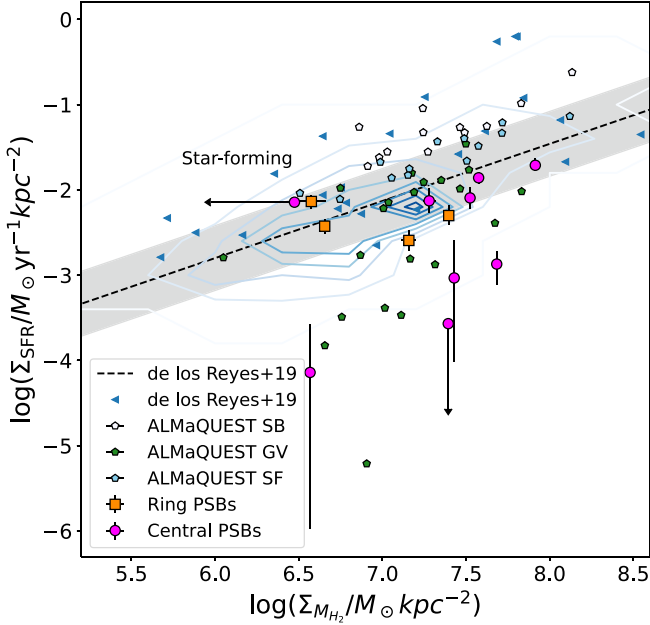


**Figure 8.** The Kennicutt–Schmidt relation between star formation surface density and molecular gas surface density for the PSB regions in our sample in purple for cPSB galaxies and orange for rPSB galaxies. We plot the ALMaQUEST SF, GV, and SB galaxies as blue, green, and white pentagons, respectively. The dashed line shows the measured relation from de los Reyes & Kennicutt (2019) with the estimated scatter shaded in gray.

such as AGN-driven outflows. We plot the molecular gas fraction as a function of the time since starburst, burst mass fraction, and fraction of stellar mass formed in the last gigayear ( $F_{1 \text{ Gyr}}$ ) for our PSB regions in Figure 10. The time since starburst is the lookback time when the peak of the burst

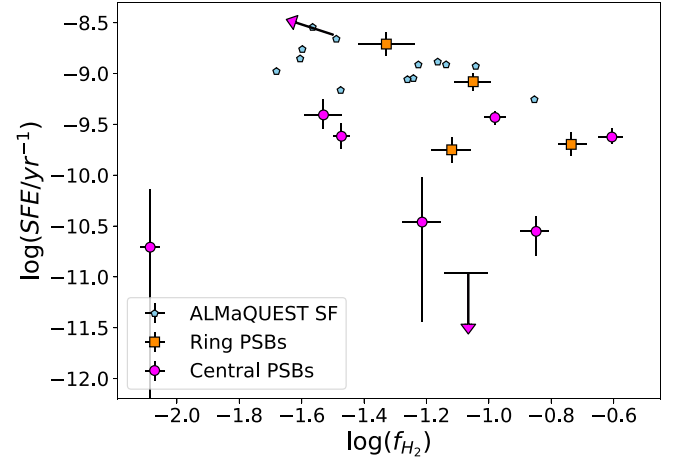


**Figure 9.** The SFE ( $\text{SFR}/M_{\text{H}_2}$ ) and molecular gas fraction ( $M_{\text{H}_2}/M_*$ ) for PSB regions (cPSB galaxies in purple, and rPSB galaxies in orange) and the ALMaQUEST star-forming galaxies. The downward arrow shows an upper limit in SFR, and the diagonally pointing arrows show an upper limit in  $M_{\text{H}_2}$  with constant SFR and  $M_*$ .

occurs, consistent with the definition of  $t_{\text{burst}}$  in Equation (2) and from Wild et al. (2020).

With our small sample, we do not observe any evolution in molecular gas fraction after the starburst, burst mass fraction, or the fraction of stellar mass formed in the last gigayear. To determine whether any of these correlations are statistically significant, we use Kendall’s  $\tau$  rank correlation coefficient, a nonparametric correlation test that typically yields similar results as Spearman’s  $\rho$ . As discussed in Feigelson & Babu (2012), this coefficient can be generalized to include upper limits, as is necessary with our CO non-detection. We find no statistically significant correlations between molecular gas

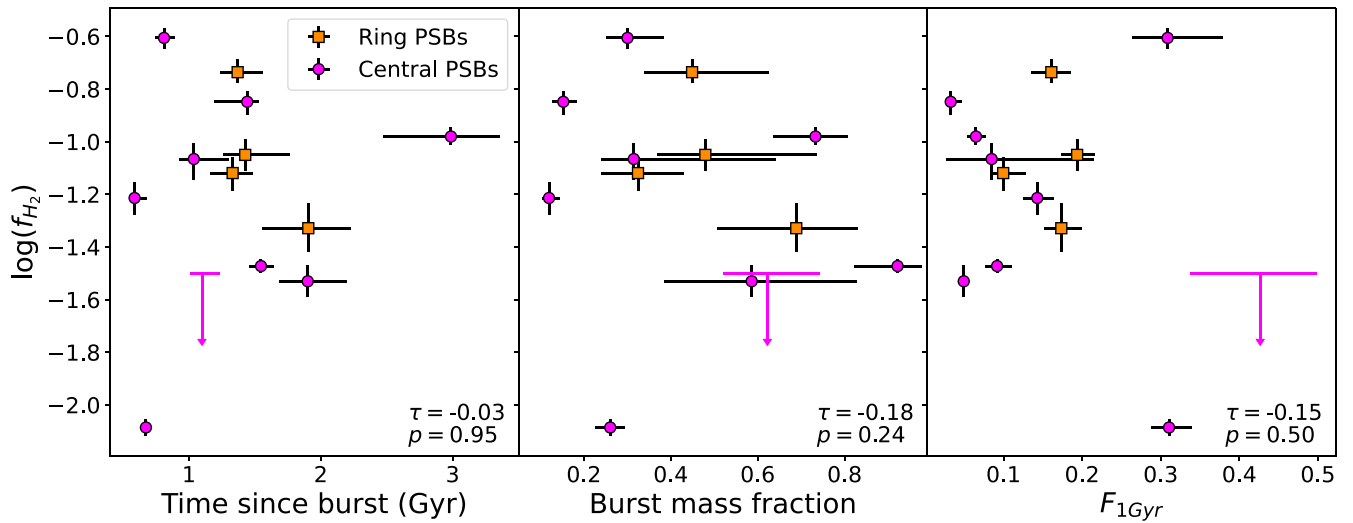


**Figure 10.** Correlations between the log molecular gas fraction ( $M_{\text{H}_2}/M_*$ ) of PSB regions and SFH parameters. cPSB galaxies are plotted in purple and rPSB galaxies in orange. Kendall’s  $\tau$  correlation coefficient (including upper limits) and accompanying  $p$ -value are shown in the bottom right of each panel. We do not observe a significant correlation between any of the plotted quantities. Left: log molecular gas fraction vs. the time since the burst, approximately the time since the peak of the starburst. Center: log molecular gas fraction and the fraction of stellar mass formed in the recent starburst. Right: log molecular gas fraction and the fraction of stellar mass formed in the last Gyr.

fraction and the plotted SFH parameters in Figure 10. However, our sample is small and heterogeneous with both cPSB galaxies and rPSB galaxies, so any correlations may be washed out by the intrinsic scatter of the relation, such as the range of gas fractions before the PSB phase. We might expect a correlation between the gas fraction and the burst mass fraction and  $F_{1\text{Gyr}}$  if gas removal is driven by exhaustion of gas reservoirs in the starburst. However, we observe no such correlation, though this may again be due to the small size of our sample.

To determine whether the overall ISM content of our PSB galaxies is evolving, we attempt a similar analysis with H I gas mass measurements from the H I-MaNGA survey (Stark et al. 2021) in Appendix H, but are unable to draw conclusions due to a lack of H I measurements with low source confusion probabilities in our sample.

#### 4.5. Emission-line Diagnostics

We classify the ionization source of the gas in our galaxies using the Baldwin, Phillips, and Terlevich diagram (BPT; diagram Baldwin et al. 1981) and the  $W(\text{H}\alpha)$  versus  $[\text{N II}]/\text{H}\alpha$  (WHAN) diagram (Cid Fernandes et al. 2011). Figure 11 shows both diagrams for each galaxy, along with the ionization source classifications overlaid on the SDSS 3-color image for both diagrams. We require each line to have an  $\text{S/N} \geq 3$ . We classify AGN spaxels with the BPT diagram as above the Kewley et al. (2001) line, and composite spaxels as below this line but above the Kauffmann et al. (2003a) line. In the WHAN diagram, strong and weak AGN spaxels have  $[\text{N II}]/\text{H}\alpha > 0.4$  while strong AGN spaxels have  $W(\text{H}\alpha) > 6 \text{ \AA}$ , weak AGN have  $W(\text{H}\alpha) > 3 \text{ \AA}$ , and retired spaxels have  $W(\text{H}\alpha) < 3 \text{ \AA}$ . These retired spaxels are ionized by hot low-mass evolved stars (HOLMES). With only optical emission lines, it is difficult to unambiguously separate AGN and shock ionization (e.g., Alatalo et al. 2016b; Kewley et al. 2019). However, given the central location of an AGN, off-center AGN-classified spaxels in both diagrams are likely to be ionized from shocks (Kewley et al. 2019).

Three galaxies are dominated by star-forming spaxels in both diagrams: 8083-12703, 8085-6104, and 8086-3704. All three of these galaxies also have off-center BPT composite spaxels and WHAN strong/weak AGN spaxels, a likely sign of shock ionization. Five galaxies are dominated by retired spaxels in the WHAN diagram, corresponding to AGN/composite BPT spaxels: 7964-1902, 8081-3702, 8655-1902, 8941-3701, and 9494-3701. While 8655-1902 does have some central weak AGN spaxels, the diagram shows these spaxels are close to the border with the retired classification, making it difficult to differentiate between these two ionization sources. Finally, the remaining five galaxies have central regions dominated by BPT AGN or composite spaxels and WHAN strong AGN spaxels: 8655-3701, 8982-6104, 8080-3704, 9088-9102, and 9194-3702. The spatial extent of the AGN ionization varies; 8655-3701 consists of almost entirely WHAN strong and weak AGN spaxels, whereas the other galaxies have a central core of WHAN strong AGN spaxels surrounded by a ring of weak AGN spaxels and then retired spaxels. Three of these central AGN galaxies also have isolated islands of off-center WHAN strong AGN spaxels: 8982-6104, 9088-9102, and 9194-3702, which again may be ionized from shocks.

Overall, we find that ionization in 4–5/9 our cPSB galaxies is driven by HOLMES, 3–4/9 by AGN, and star formation in 1/9, where 8655-1902 is an ambiguous case where HOLMES or a weak AGN could be contributing to central ionization. The percentage of 33%–44% cPSB AGN hosts is broadly consistent with previous work that has found that a central supermassive black hole is an AGN for approximately 50% of the PSB phase. Finally, 4/9 of our cPSB galaxies show evidence of noncentral shock ionization.

As for our rPSB galaxies, 2/4 have central star formation with noncentral shocks, and the other 2/4 are ionized by an AGN. Our small sample of rPSB galaxies similarly has a high AGN fraction. The former two galaxies are rPSB galaxies; this ionization pattern is consistent with the centers of these rPSB galaxies being under typical star-forming conditions with shocks or other energetic processes ionizing and disrupting gas in the outskirts.

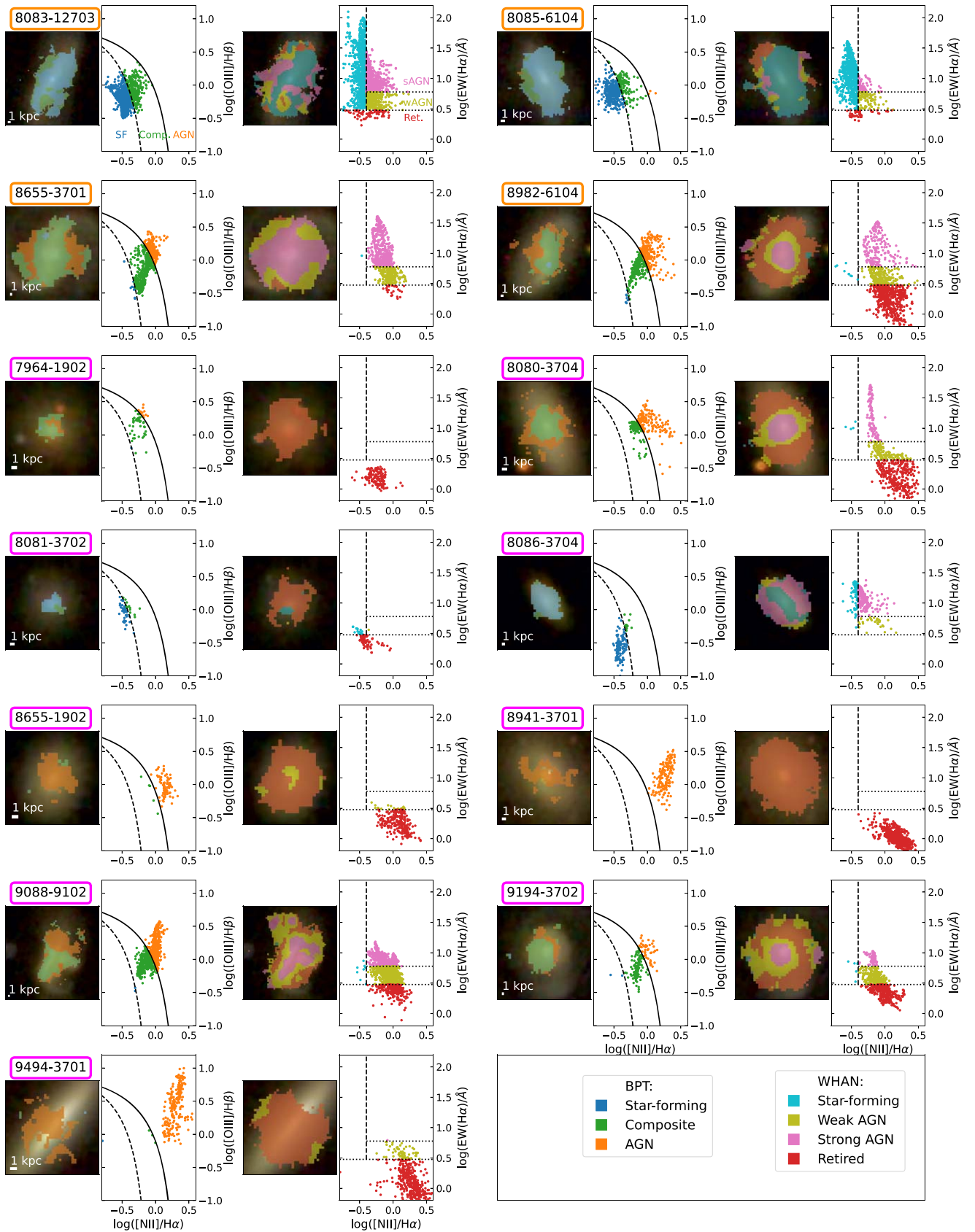


**Figure 11.** Spatially resolved [N II] BPT diagrams and WHAN diagrams for each galaxy. Left: SDSS 3-color image with composite, AGN, and star-forming classified spaxels in green, orange, and blue respectively, next to the [N II]/H $\alpha$  vs. [O III]/H $\beta$  diagram for each galaxy with the same coloring. The solid black line represents data from Kewley et al. (2001), and the dashed line is from Kauffmann et al. (2003a). Right: SDSS 3-color image with star-forming, weak AGN, strong AGN, and retired classified spaxels in teal, brown, pink, and red, respectively, alongside the WHAN diagram, W(H $\alpha$ ) vs. [N II]/H $\alpha$  with classification boundaries from Cid Fernandes et al. (2011).

## 5. Discussion

### 5.1. A Tumultuous History for PSBs

Overall, centrally concentrated molecular gas reservoirs and disturbed stellar kinematics in 7/13 PSB galaxies provide strong evidence that these galaxies have undergone a recent merger. For 8/13 of our PSB galaxies, the majority of the CO emission resides in a central core that is unresolved with our kiloparsec-scale resolution CO observations. Though few other PSB galaxies have spatially resolved CO observations, other studies also reveal highly centrally concentrated molecular gas distributions (Smercina et al. 2022). Even with higher resolution CO observations (down to  $\sim 200$  pc spatial resolution) Smercina et al. (2022) are still unable to resolve the central cores containing the majority of the molecular gas in a sample of six PSB galaxies. These centrally concentrated CO morphologies are consistent with predictions from Davis et al. (2019). By studying galaxies that have undergone a recent PSB phase in the EAGLE simulation, they find that EAGLE PSB galaxies tend to have centrally concentrated molecular gas reservoirs and disturbed kinematics primarily due to mergers disrupting the gas and driving it inward, sometimes resulting in a starburst or an increase in AGN accretion, both of which deplete molecular gas reservoirs quickly.

Asymmetric or disordered stellar velocity fields further support a merger history for 7/13 of our cPSB galaxies. While kinematic features such as stellar bars, oval distortions, and disk warps (which may also be of merger origin) could lead to symmetric alterations to the stellar velocity fields, tidal interactions from mergers are the most likely cause of stellar asymmetries. These disturbances are not limited to the stellar velocity field, as the molecular gas reservoirs in four of our PSB galaxies lack rotation, indicating that the molecular gas reservoirs themselves are disturbed. Of the 12 ALMaQUEST star-forming galaxies, only two have stellar velocity fields with asymmetric Radon profiles, and all 12 have consistent CO, stellar, and  $H\alpha$  PAs, in comparison to only 5/12 PSB galaxies. Thus, the kinematics of our PSB galaxies are less orderly and more disturbed than in the ALMaQUEST star-forming sample, indicating that physical processes disturbing kinematics in our galaxies are more prevalent. Four of our PSB galaxies are visually classified as either post-mergers (8083-12703, 8655-3701, and 9194-3702) by Thorp et al. (2019), or ongoing mergers (9088-9102). The stellar Radon profiles of all four of these galaxies are either asymmetric or could not be classified due to a lack of rotation.

A substantial body of work supports gas-rich mergers leading to a starburst and subsequent quenching episode resulting in a PSB phase. In multiple simulations, a majority of PSB galaxies have recently undergone mergers, making them an important formation mechanism (Lotz et al. 2004; Davis et al. 2019; Zheng et al. 2020). Observationally, PSB galaxies are morphologically disturbed and show tidal features at higher rates than typical star-forming or ETGs (Yang et al. 2008; Sazonova et al. 2021), further supporting a recent merger for at least half of local PSB galaxies.

While mergers may drive the bulk of the observed stellar asymmetries, smaller interactions or outflows may drive star formation suppression in the 3/12 of our PSB galaxies with symmetrical stellar Radon profiles and misaligned or asymmetric  $H\alpha$  Radon profiles. A minor merger or interaction event could trigger a starburst and the following PSB phase

(Wilkinson et al. 2018), which could result in the misalignment of the gas without significantly altering the stellar rotation. Alternatively, an outflow could drive a disturbance in the gas while leaving the stellar velocity field intact. Outflows have previously been observed in PSB galaxies (e.g., Alatalo et al. 2011; Luo et al. 2022; Smercina et al. 2022), though the overall prevalence and impact of outflows on PSB evolution are not well understood. In particular, it is unclear whether the primary effect of an outflow is to expel gas from a PSB (e.g., Feruglio et al. 2010; Baron et al. 2017), or if the outflowing gas remains in the galaxy but disturbs the galaxy's gas reservoir, resulting in suppressed star formation (e.g., Alatalo et al. 2011; Luo et al. 2022).

We find evidence of an outflow ejecting molecular gas from the center in one of our PSB galaxies, 9494-3701. This is an edge-on disk galaxy with constant stellar and  $H\alpha$  Radon profiles, though the  $H\alpha$  PA is misaligned approximately  $90^\circ$  from the disk, as shown in Figure 5. The CO morphology in Figure 3 shows significant extraplanar gas also perpendicular to the disk, which together appears to be a multiphase outflow. However, we do not see evidence of this outflow in the CO line profile (Figure 3) or the position velocity ( $P-V$ ) diagram (shown in Appendix E), potentially because this extraplanar gas is too faint. The low molecular gas fraction ( $< 1\%$ ) of the cPSB region may indicate that gas expulsion from the central region is contributing to quenching. More investigation is needed to determine whether the outflows are powerful enough to eject the gas from the galaxy, and if the outflow itself is driving the quenching of the galaxy or if another physical process (such as an AGN) drives both the outflow and the central quenching.

It is unclear whether this is an AGN or starburst-driven outflow. The WHAN diagram in Figure 11 shows that 9494-3701 is dominated by retired spaxels and is thus ionized primarily by HOLMES. However, given that the duty cycle of AGN is much shorter than the length of a PSB phase, it is possible that 9494-3701 previously hosted an AGN that has since shut off. Alternatively, though the current central region star formation surface density in the PSB region is very low ( $\log \Sigma_{\text{SFR}} = -4.1 M_\odot \text{ yr}^{-1} \text{ kpc}^{-2}$ ), the recent starburst in this galaxy could have triggered the outflow and since quenched. Other galaxies in our sample with misaligned or disturbed gas kinematics, such as 8080-3704, 8655-1902, and 8941-3701 may also have outflows with masses too small to be detected with our CO data. Detailed spectral fitting with high spectral resolution IFU data could provide strong outflow evidence in these galaxies.

Finally, we turn our attention to three galaxies without signs of stellar or gas kinematic disturbance of the aforementioned galaxies: 8085-6104, 8086-3704, and 8982-6104. In principle, a number of processes could be driving their current PSB phases, including minor mergers or interactions, stellar bars, AGN feedback, or environmental processes like ram pressure stripping. While none of these galaxies currently show obvious signs of a merger, 8086-3704 is our oldest PSB with a burst time of  $3.0^{+0.4}_{-0.5}$  Gyr, so it is possible that the gas and stars have settled since a previous merger.

Alternatively, stellar bars could cause our observed centrally concentrated molecular gas reservoirs and star formation suppression. Bars can drive gas inflows, funneling gas inward to the center of the galaxy (e.g., Regan et al. 1997; Athanassoula et al. 2013; Querejeta et al. 2016). Bars can also



suppress star formation in the disk (e.g., Vera et al. 2016; Kruk et al. 2018), and may lead to increased star formation in the gas-rich nuclear region (e.g., George et al. 2019).

Only one of our galaxies has a strong bar, 8655-3701. The bar is present in the SDSS image, and the  $P$ - $V$  diagram of the CO emission shows the characteristic “X” shape associated with a bar, shown in Appendix E. Salim et al. (2020) find that a rotating bar in NGC 7674, a Hickson compact group galaxy, likely drives turbulence leading to suppressed star formation in the bar region. While the nucleus of 8655-3701 is strongly star forming, the ends of the bar are co-incident with PSB regions. This quenching morphology is consistent with the rotation of the star formation suppressing turbulence as seen in NGC 7674, though these two galaxies reside in very different environments. Higher resolution CO observations that can resolve the scale height of the gas for reliable velocity dispersion measurements are needed to confirm whether the bar is driving turbulence in this galaxy, and whether such turbulence is co-spatial with quenching regions. It is also possible that the WHAN and BPT-classified AGN spaxels away from the center of this galaxy are from shocks that could be driven by the rotation of the bar, as has been observed in other strongly barred galaxies (e.g., Athanassoula 1992).

While it is possible that other galaxies in our sample have weak bars undetected with the SDSS imaging, it is unclear whether a weak bar could drive star formation suppression to the same extent as a strong bar, though bar length may be more important than bar strength (Fraser-McKelvie et al. 2020; Géron et al. 2021). The three galaxies without signs of kinematic disturbance (i.e., lacking asymmetrical stellar or  $H\alpha$  Radon profiles and having kinematically aligned CO, stars, and  $H\alpha$ ), 8085-6104, 8086-3704, and 8982-6104, all have inner bends in their stellar Radon profiles. Stark et al. (2018) found that stellar bars are the primary driver of inner bends in stellar Radon profiles, so a weak bar contributing to star formation suppression in these galaxies is possible.

### 5.2. Gas Stabilization

Figure 9 shows that a substantial fraction of our PSB regions have significant gas reservoirs but suppressed star formation. This result is in good agreement with the global properties of PSB galaxies from previous spatially unresolved studies (Rowlands et al. 2015; French et al. 2018), but with our spatially resolved observations, we are considering only the PSB regions of our galaxies. Thus, our extension of this result indicates that within a PSB, there is still a significant amount of gas in the quenching PSB region that is stabilized against star formation. We also see evidence of suppressed SFE when comparing our galaxies to other star-forming samples along the Kennicutt–Schmidt relation, shown in Figure 8. The majority of our PSB galaxies are below the relation measured by de los Reyes & Kennicutt (2019), with our cPSB galaxies showing an especially large offset despite large molecular gas surface densities. Though the source of this suppression is still unclear, shocks and turbulence driven by AGN feedback can plausibly suppress star formation.

Shocks can regulate star formation as their excess kinetic energy makes the gravitational collapse of molecular clouds needed for star formation more difficult, thus decreasing SFE. The suppressive impact of shocks has been observed in a variety of studies, and in AGN host galaxies in particular (e.g., Alatalo et al. 2014; Aalto et al. 2015; Alatalo et al. 2015a;

Guillard et al. 2015). Three of our galaxies have significant WHAN-classified star-forming centers with regions of off-center WHAN-classified AGN spaxels, consistent with shock ionization: 8083-12703, 8085-6104, and 8086-3704. Three other galaxies have central AGN with separated off-center regions of AGN spaxels, consistent with AGN-driven shocks: 8982-6104, 9088-9102, and 9194-3702. The possible presence of shocks in 6/13 of our PSB galaxies is suggestive, though from our data it is difficult to determine what the source of these shocks is. Half of our shock candidates have AGN, indicating that AGN outflows could contribute to shocks. In other galaxies, it is possible that the AGN has since shut off but the outflows are still creating shocks. Mergers can also lead to shocks, which may be the case in 9088-9102 which is an ongoing merger. Finally, star formation can drive outflows and shocks, as may be in the case of 8083-12703 and 8085-6104. To unravel the impacts of shocks in our galaxies, we first must confirm these galaxies as shock hosts with UV and IR diagnostic lines (Kewley et al. 2019), while higher resolution CO observations will show whether shocked regions display greater star formation suppression.

Turbulence from a recent merger, outflows, or other dynamic processes such as a stellar bar can also play a suppressive role in star formation. Smercina et al. (2018) find internal turbulent pressures in three PSB galaxies  $\sim 2$  orders of magnitude greater than in typical star-forming galaxies, indicating that the extreme ISM conditions in PSB galaxies are important for understanding the suppression of star formation in these galaxies. To maintain the turbulent pressures in these galaxies, a persistent source of turbulence is required, such as AGN-driven outflows or a changing gravitational potential caused by the resettling of the potential after a merger. Thus, the tidal forces creating the observed asymmetries in the stellar velocity fields of our PSB galaxies (see Section 4.2) may lead to time-varying gravitational potentials that then drive turbulence in the gas, as observed in Arp 220, a dual nuclei merger (Scoville et al. 2017). Time-invariant stellar dynamics in bulge-dominated galaxies can also drive turbulence in the gas and suppress star formation through morphological quenching, resulting in a lack of star-forming dense gas (Martig et al. 2009, 2013). Gensior & Kruijssen (2021) find that dynamical suppression is most effective in galaxies with low gas fractions ( $< 5\%$ ) and with higher stellar masses and central concentrations. While the most massive galaxies in our sample tend to have higher gas fractions, dynamical suppression may contribute to gas stabilization in our PSB galaxies with the lowest ( $< 2\%$ ) gas fractions: 7964-1902, 8081-3702, 8941-3701, and 9494-3701, despite low stellar masses ( $< \log(10.5/M_{\odot})$ ).

Lastly, bar-driven quenching has been observed in a variety of studies as discussed in Section 5.1. With kiloparsec-scale resolution observations, we lack the spatial resolution to accurately measure the turbulent properties of the molecular gas. Expanding high-resolution CO observations to a larger sample of PSB galaxies will shed light on the impact of a turbulent medium on star formation.

The prevalence of AGN in 5/13 of our PSB galaxies makes AGN feedback an attractive gas stabilization mechanism, though higher resolution observations are needed to test this possibility. We classify five galaxies as potential AGN hosts with emission line ratios consistent with the AGN in the WHAN diagram in the central region, as shown in Figure 11.

For galaxies to quench in simulations, *radio-mode* AGN feedback is typically required to inject energy into gas reservoirs and stabilize them against gravitational collapse (Ciotti et al. 2010). Studies of individual PSBs have drawn a connection between radio-mode AGN and star formation suppression through more subtle means such as small outflows (Alatalo et al. 2015b; Luo et al. 2022). However, the low spatial resolution of our CO and optical IFU data means we cannot resolve small-scale outflows and turbulence. Piotrowska et al. (2021) find that radiatively inefficient AGN feedback drives turbulence and heats the ISM, leading to a decreased SFE. Further, they find that this AGN feedback also heats the surrounding circumgalactic medium, thus preventing accretion of cold gas and re-invigoration of star formation. To confirm these galaxies as AGN hosts, high spatial resolution radio observations or deep X-ray data are needed, though we note that a lack of radio or X-ray detection does not exclude the presence of an AGN. Other galaxies in our sample may have recently hosted AGNs that have shut off, as the duty cycle of AGN activity is much shorter than the PSB phase (Pawlik et al. 2018). Thus, the lack of current evidence for AGN activity does not eliminate the possibility that AGN feedback is important in regulating star formation in our entire sample, as found in Piotrowska et al. (2021). High-resolution, multi-wavelength observations are needed to determine the galactic-scale processes suppressing star formation and to study the impacts these mechanisms have on the cloud-scale ISM conditions governing star formation.

### 5.3. cPSBs and rPSBs

Overall, it is difficult to distinguish the quenching mechanisms active in rPSB and cPSB galaxies with our data and small sample. Chen et al. (2019) find that cPSB galaxies have a more dramatic history, while rPSB galaxies with star-forming centers may be quenching due to gas supply cutoff in the outskirts. Morphologically, cPSB and rPSB galaxies have similar mean core fractions (67% and 65%, respectively, see Figure 4). Both cPSB and rPSB galaxies show asymmetrical stellar Radon profiles (3/7 and 2/4, respectively), and both samples include galaxies with kinematic misalignments (6/9 cPSB galaxies and 1/4 rPSB galaxies). Both the cPSB and rPSB regions show evidence of star formation suppression, though to a lesser degree for the rPSB regions than some central regions, as shown in Figures 8 and 10. Finally, both samples have a significant portion of central AGN ionization (3/9 for cPSB galaxies and 2/4 for rPSB galaxies). The two rPSB galaxies without central AGN spaxels instead appear to be ionized by shocks in the outskirts of the galaxy with star formation dominating the central ionization, similar to 8086-3704, a cPSB. Overall, it appears that both cPSB and rPSB galaxies often have undergone a recent merger, given the high rate of stellar asymmetries and centrally concentrated molecular gas in both samples.

The natural question that arises is, why do some mergers appear to lead to a cPSB whereas others lead to an rPSB? Mergers can take many different forms with varying stellar mass ratios, gas fractions, and orientations all playing significant roles. More theoretical work is needed to determine the qualities that lead a merger remnant to a cPSB versus an rPSB phase. One area where we observe a difference between our cPSB and rPSB galaxies is in the gas kinematics. In Figure 6, we can see that 4/8 cPSB galaxies have asymmetric

H $\alpha$  Radon profiles, while 0/4 rPSB galaxies do. Similarly, looking at the CO velocity maps in Figure 5, 4/8 CO-detected cPSB galaxies lack significant CO rotation, whereas all four rPSB galaxies have strong CO rotation (though it is misaligned in one case). While the small sample of our rPSB galaxies makes any conclusions tentative, it appears that the gas in rPSB galaxies is less disturbed than in cPSB galaxies, potentially from a less disruptive merger or from a faster resettling of the gas. It is also possible that the highly disturbed gas in cPSB galaxies is driven by a process more commonly active in cPSB galaxies, such as outflows.

Our conclusion that mergers are important in the formation of both cPSB and rPSB galaxies is consistent with that of Chen et al. (2019). With the addition of our spatially resolved CO observations, we find that the gas appears to be less disturbed in rPSB galaxies, showing stronger rotation and more symmetrical velocity maps. Chen et al. (2019) differentiate between two types of rPSB galaxies, those that are experiencing a global shutdown of star formation, and those with star-forming centers. They conclude that the former group may be quenching from a lack of gas inflow, while the latter likely have experienced either ram pressure stripping or a merger/interaction. Owers et al. (2019) also identify galaxies with central star formation and PSB signatures in the outskirts, though they find these galaxies almost exclusively in a cluster context, and conclude that the outer PSB regions are driven by ram pressure stripping. Our rPSB galaxies similarly have star-forming centers and outer PSB regions. However, the PSB regions in our rPSB galaxies have gas fractions similar to the cPSB regions and ALMaQUEST star-forming galaxies, indicating that a lack of molecular gas is not driving quenching. The primary difference Chen et al. (2019) find between their cPSB and rPSB galaxies is in their SFHs and rotational support, where cPSB galaxies have a more mixed-age stellar population throughout the galaxy, and also have less rotational support, both of which indicate a recent dramatic event such as a merger. Our results show stellar disturbances in both cPSB and rPSB galaxies, indicating a common merger origin, but the molecular and ionized gas in cPSB galaxies appears to be more disturbed than in rPSB galaxies, hinting at the importance of gas disruption through processes such as outflows.

It is tempting to point toward rPSB galaxies as outside-in quenching systems and cPSB galaxies as inside-out quenching systems, but this simplistic picture has a number of flaws. It is unclear whether rPSB galaxies can truly be considered *quenching* systems, as their evolution is unknown: will the outskirts of these galaxies eventually undergo re-invigoration of their star formation, or is an rPSB phase the first step toward outside-in quenching? To answer this question, a larger sample of rPSB galaxies is needed with a range of post-burst ages, as well as an improved theoretical understanding of how rPSB galaxies form and evolve. Integral Field Spectroscopy (IFS) studies of cPSB galaxies have enabled measurements of radial gradients in stellar populations. Chen et al. (2019) find that the outskirts of cPSB galaxies show weaker PSB signatures than the central regions, indicating that these regions either never underwent a starburst or that the burst was weaker or older. Zheng et al. (2020) use binary merger simulations to measure radial gradients in cPSB galaxies and find that the starburst peaks at the same time throughout the galaxy, but is more prolonged and stronger in the center, leading to the radial gradients observed in Chen et al. (2019). In our sample, one of

our cPSB galaxies, 8941-3701, has a cPSB region and the outskirts of the galaxy are quiescent but not PSB, which is consistent with outside-in quenching. More detailed spatially resolved spectral fitting on a larger sample will show whether this qualitative outside-in behavior is typical.

## 6. Conclusions

In this work, we have presented ALMA CO(1–0) observations of 13 PSB galaxies with accompanying MaNGA optical IFS data, nine of which have cPSB regions and four with ring outskirt PSB regions. With these data, we study the molecular gas morphology, kinematics, and star formation properties of these galaxies to work toward understanding the causes and mechanisms of star formation quenching in these galaxies. We list our primary conclusions below:

1. *The majority of our PSB galaxies show evidence of a recent merger.* 7/13 PSB galaxies have asymmetric or nonrotating stellar velocity fields, consistent with tidal forces from a merger or interaction disrupting the stellar kinematics. The remaining six galaxies lack kinematic evidence of a recent merger. While mergers resulting in symmetric stellar disturbances (such as a disk warp) and minor mergers are not ruled out, other processes such as outflows and weak stellar bars may play a role in the quenching of these galaxies, as we see in the outflow host 9494-3701.
2. *Significant molecular gas reservoirs in PSB regions are stabilized against star formation.* Within the PSB regions of our galaxies, we find typical molecular gas fractions but low SFEs in nearly half of our sample. PSB galaxies then do not typically quench due to a lack of molecular gas but because the existing gas is not forming stars. AGN feedback may drive this stabilization, with 5/13 galaxies hosting central AGN-like emission.
3. *cPSB and rPSB regions have similar properties, though gas in rPSB galaxies may be less disturbed.* The PSB regions of our cPSB and rPSB regions have similar star formation and molecular gas properties. Both samples have approximately half of galaxies with evidence of mergers (3/7 cPSB galaxies and 2/4 rPSB galaxies). However, both the ionized and molecular gas in rPSB galaxies appears to be less disturbed than that of the cPSB galaxies, which may hint at different merger conditions or another process primarily impacting cPSB galaxies, such as outflows.

We thank the anonymous referee for helpful comments that improved this work. We also thank Jindra Gensior for constructive scientific comments.

J.O., Y.L., K.A., K.R., and E.S. have been partially funded by Space Telescope Science Institute Director’s Discretionary Research Fund grants D0101.90241, D0101.90276, D0101.90262, D0101.90281, D0101.90296, HST grants GO-14715.021, GO-14649.015, and Chandra grant GO7-18096A. J.O. acknowledges support from NRAO under grant No. SOSPA7-027. L.L. thanks the support from the Academia Sinica under the Career Development Award CDA107-M03 and the Ministry of Science & Technology of Taiwan under the grant MOST 111-2112-M-001-044. H.A.P. acknowledges support by the National Science and Technology Council of Taiwan under grant 110-2112-M-032-020-MY3. W.B.

acknowledges support from the Science and Technology Facilities Council (STFC). The Cosmic Dawn Center is funded by the Danish National Research Foundation under grant No. 140. R.A.R. acknowledges the support from Conselho Nacional de Desenvolvimento Científico e Tecnológico and Fundação de Amparo à pesquisa do Estado do Rio Grande do Sul. TAD acknowledges support from the UK Science and Technology Facilities Council through grants ST/S00033X/1 and ST/W000830/1. FvdV was supported by a Royal Society University Research Fellowship.

The National Radio Astronomy Observatory is a facility of the National Science Foundation operated under cooperative agreement by Associated Universities, Inc.

This paper makes use of the following ALMA data: ADS/JAO.ALMA#2019.1.01136.S. ALMA is a partnership of ESO (representing its member states), NSF (USA) and NINS (Japan), together with NRC (Canada), MOST and ASIAA (Taiwan), and KASI (Republic of Korea), in cooperation with the Republic of Chile. The Joint ALMA Observatory is operated by ESO, AUI/NRAO and NAOJ.

Funding for SDSS-IV has been provided by the Alfred P. Sloan Foundation, the U.S. Department of Energy Office of Science, and the Participating Institutions.

SDSS-IV acknowledges support and resources from the Center for High Performance Computing at the University of Utah. The SDSS website is at [www.sdss.org](http://www.sdss.org).

SDSS-IV is managed by the Astrophysical Research Consortium for the Participating Institutions of the SDSS Collaboration including the Brazilian Participation Group, the Carnegie Institution for Science, Carnegie Mellon University, Center for Astrophysics—Harvard & Smithsonian, the Chilean Participation Group, the French Participation Group, Instituto de Astrofísica de Canarias, The Johns Hopkins University, Kavli Institute for the Physics and Mathematics of the Universe (IPMU)/University of Tokyo, the Korean Participation Group, Lawrence Berkeley National Laboratory, Leibniz Institut für Astrophysik Potsdam (AIP), Max-Planck-Institut für Astronomie (MPIA Heidelberg), Max-Planck-Institut für Astrophysik (MPA Garching), Max-Planck-Institut für Extraterrestrische Physik (MPE), National Astronomical Observatories of China, New Mexico State University, New York University, University of Notre Dame, Observatório Nacional/MCTI, The Ohio State University, Pennsylvania State University, Shanghai Astronomical Observatory, United Kingdom Participation Group, Universidad Nacional Autónoma de México, University of Arizona, University of Colorado Boulder, University of Oxford, University of Portsmouth, University of Utah, University of Virginia, University of Washington, University of Wisconsin, Vanderbilt University, and Yale University.

*Facilities:* ALMA, Sloan.

*Software:* This research has made use of the CIRADA cutout service at [URL.cutouts.cirada.ca](http://URL.cutouts.cirada.ca), operated by the Canadian Initiative for Radio Astronomy Data Analysis (CIRADA). CIRADA is funded by a grant from the Canada Foundation for Innovation 2017 Innovation Fund (Project 35999), as well as by the Provinces of Ontario, British Columbia, Alberta, Manitoba and Quebec, in collaboration with the National Research Council of Canada, the US National Radio Astronomy Observatory and Australia’s Commonwealth Scientific and Industrial Research Organization. We use the NADA package in R to compute the Kendall’s  $\tau$  coefficients and accompanying  $p$ -values. Astropy (Astropy Collaboration et al.

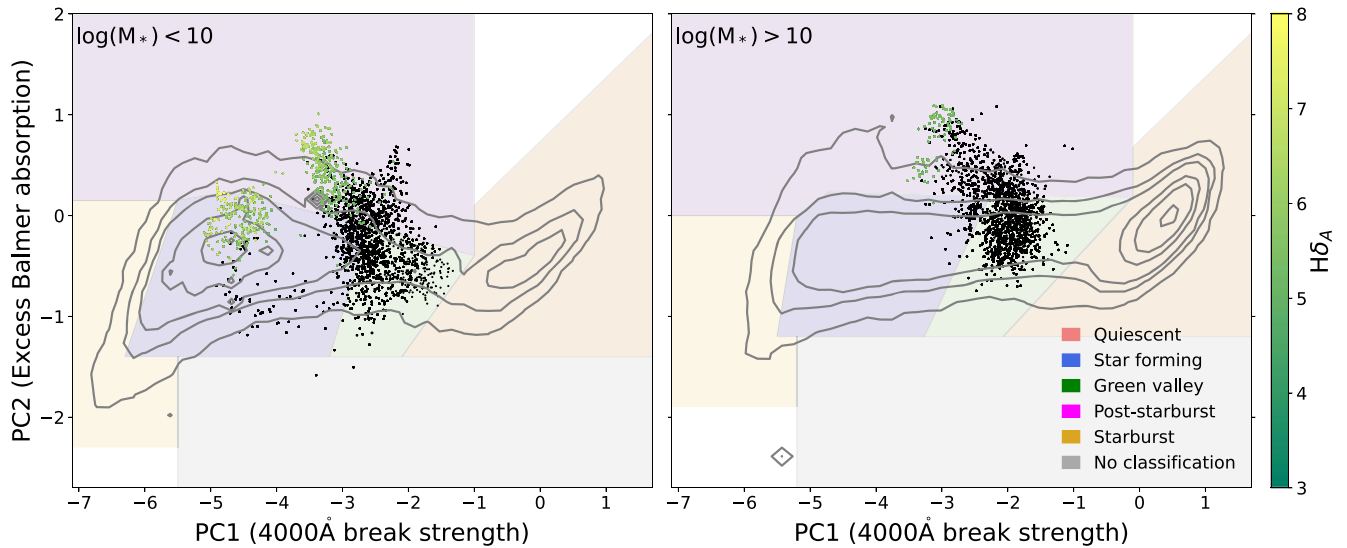


**Figure 12.** PCA classification boundaries in PC1 ( $D_n4000$ ) and PC2 (excess Balmer absorption). The shaded regions show the boundaries for quiescent (red), SF (blue), GV (green), PSB (purple), and SB (yellow) classifications. The gray contours show the parent DR15 MaNGA sample, with levels corresponding to 1%, 5%, 30%, 50%, and 90% of the largest bin. The black and colored points show all spaxels from galaxies in the Chen et al. (2019) and PCA combined sample. The colored points are spaxels within those galaxies that are classified as PSB with the Chen et al. (2019) selection method, and are color coded according to their  $H\delta_A$ .

2013, 2018), CASA v6.4.3; McMullin et al. 2007), celerite2 (Foreman-Mackey et al. 2017; Foreman-Mackey 2018), mangadap (Westfall et al. 2019), Marvin (Cherinka et al. 2019), matplotlib (Hunter 2007), NumPy (Harris et al. 2020), PaFit (Krajinović et al. 2006), statmorph (Rodriguez-Gomez et al. 2019).

### Appendix A PCA Classification Boundaries

We show the classification boundaries for the PCA analysis in Figure 12. The boundaries differ for low and high mass spaxels (defined as above and below  $M_* = 10^{10} M_\odot$ ) as PC1 and PC2 values have a weak stellar mass dependence. We modified the original boundaries from Rowlands et al. (2018) visually to optimize the agreement between the PCA method and the Chen et al. (2019) selection method while minimizing contamination. We plot all spaxels from the final Chen et al. (2019) and PCA combined sample in Figure 12, and color spaxels identified as PSB by Chen et al. (2019) in green according to their  $H\delta_A$  value. In the high mass case, all Chen et al. (2019) PSB-classified spaxels are also PSB classified with the PCA method, though for spaxels in low stellar mass galaxies there is overlap with the star-forming classification region.

Different PSB selection methods result in samples with different properties, including post-burst ages and AGN or shock presence, and no single selection will include all galaxies considered to be PSB.

### Appendix B 8939-3703: A Star-forming Interloper

As mentioned in Section 2.2, our spectral fitting results of 8939-3703 indicate that this galaxy is a star-forming interloper. We plot the SFH of this galaxy in Figure 15, where we see relatively constant star formation over the last  $\sim 3$  Gyr. Since the residuals are in line with Gaussian random noise and the fitted GP term is well behaved, the optical continuum for this galaxy is well fit. The derived SFH indicates that there is little

evidence in the continuum that a recent starburst nor rapid quenching occurred in the PSB spaxels.

This galaxy is selected as a PSB using the PCA method of Rowlands et al. (2018), though we note it is not selected in the sample of Chen et al. (2019). Figure 13 shows the SDSS 3-color image, the PCA spaxel classifications, and the excess Balmer absorption of 8939-3703. The high values of excess Balmer absorption mean that many spaxels in this galaxy are not close to the PSB classification boundary in  $D_n4000$  and Balmer absorption space (principal components 1 and 2, respectively, in our PCA analysis). In the optical image, we do see that a foreground star is close to the galaxy. However, there is no visible diffraction spike in the MaNGA data and all the quality flags indicate this star did not contaminate the data.

We do not detect any CO(1–0) emission from this galaxy with ALMA. We measure an upper limit molecular gas mass of  $\log M_{H_2}/M_\odot < 7.7$ .

### Appendix C Different Values of $\alpha_{CO}$

Observationally, Smercina et al. (2018) find that an  $\alpha_{CO}$  of  $4 M_\odot (K km s^{-1} pc^2)^{-1}$  was generally in agreement with molecular gas masses derived from fitting multiple  $H_2$  rotational emission lines for a sample of E+A galaxies. However, their requirement of  $W(H\alpha) < 3 \text{ \AA}$  for their sample would likely exclude 8/13 galaxies in our sample, so we investigate the impact of a varying  $\alpha_{CO}$  on our results.

The unique ISM conditions in PSB galaxies make determining the proper conversion from CO line flux to molecular gas mass, i.e.,  $\alpha_{CO}$  difficult. Primary factors that can alter  $\alpha_{CO}$  include metallicity and the galactic environment—often including starbursting galaxies and mergers (e.g., Bolatto et al. 2013). Narayanan et al. (2012) combine these two impacts in a single prescription for  $\alpha_{CO}$ :

$$\alpha_{CO} = \frac{\min[6.3, 10.7 \times \langle W_{CO} \rangle^{-0.32}}{Z^{0.65}} \quad (C1)$$

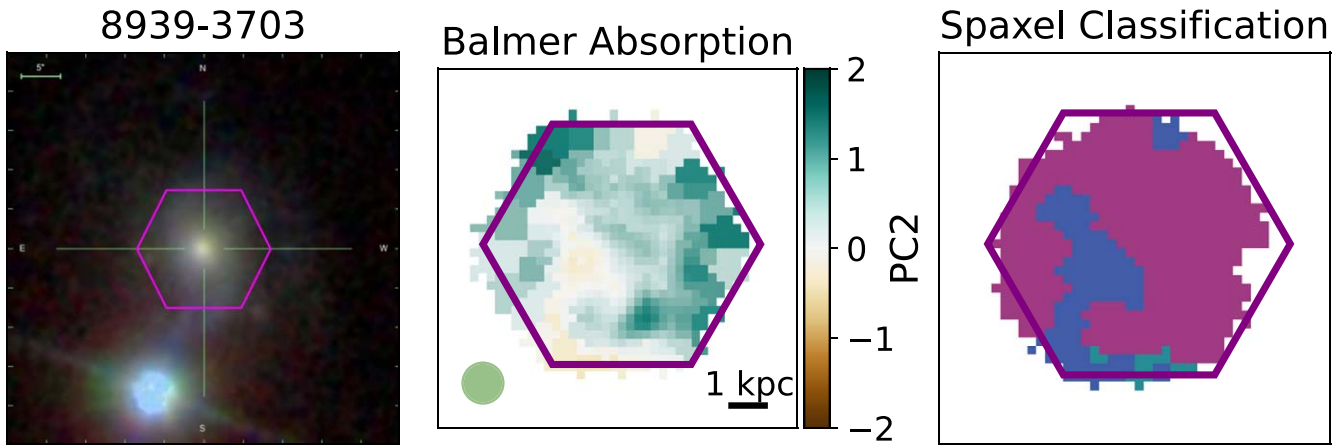


**Figure 13.** PCA classification results for 8939-3703. Left: the SDSS 3-color image, with a clear foreground star. Center: the excess Balmer absorption of each spaxel. Teal regions correspond to greater Balmer absorption, and to PSB regions. Right: the PCA classification from Rowlands et al. (2018), with PSB spaxels in purple, star-forming spaxels in blue, and starburst spaxels in teal. The green circle shows the MaNGA 2''/5 average seeing. This galaxy is clearly classified as a PSB.

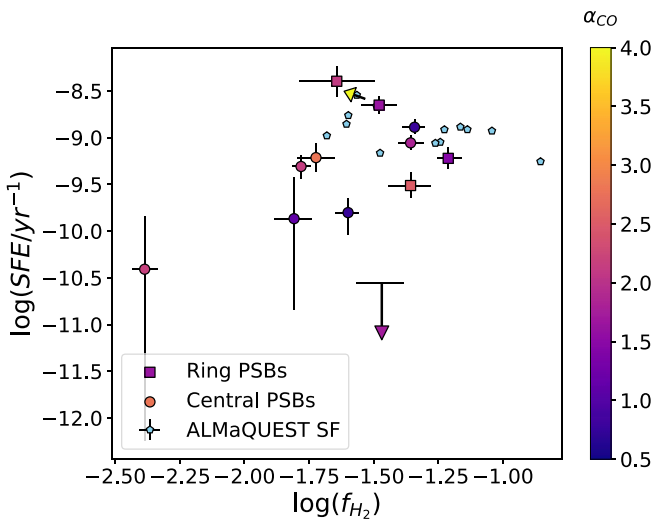


**Figure 14.** SFEs and molecular gas fractions computed with a varying  $\alpha_{\text{CO}}$  from Narayanan et al. (2012) for the PSB regions in our sample, with  $Z' = 2$ . PSB regions of cPSB galaxies are plotted as circles, and PSB regions of rPSB galaxies are plotted as squares. These markers are colored by their computed  $\alpha_{\text{CO}}$  value. We also plot ALMaQUEST star-forming galaxies, with a Milky Way  $\alpha_{\text{CO}}$  of  $4.35 M_{\odot} (\text{K km s}^{-1} \text{pc}^2)^{-1}$ .

where  $\langle W_{\text{CO}} \rangle$  is the CO surface brightness measured in  $\text{K km s}^{-1}$ , and  $Z'$  is the gas-phase metallicity normalized by the solar metallicity. While we directly measure the CO surface brightness, determining the gas-phase metallicity is difficult in the non-star-forming spaxels of our PSB galaxies, though work is being done to extend metallicity relations to LI(N)ER regions (Kumari et al. 2021). Goto (2007) find that the metallicities of a sample of 451 E+A are consistent with solar metallicities. Given that AGNs appear to be present in about four of our galaxies (see Section 4.5) and would not be included in the E+A sample of Goto (2007), we also consider that the typical metallicity of AGN hosts can range from near-solar values to up to a few times solar metallicity (e.g., Hamann et al. 2002). We conservatively assign a metallicity of 2 times solar (i.e.,  $Z' = 2$ ) for our sample and compute new  $\alpha_{\text{CO}}$  values for our PSB regions. The mean  $\alpha_{\text{CO}}$  of our PSB regions using Equation (C1) is  $1.9 M_{\odot} (\text{K km s}^{-1} \text{pc}^2)^{-1}$ , which is within a reasonable uncertainty of a Milky Way  $\alpha_{\text{CO}}$  of  $4.35 M_{\odot} (\text{K km s}^{-1} \text{pc}^2)^{-1}$  of a factor of a few. Alternatively, if our PSB

**Table 5**  
Model Priors Used for Spectral Fitting of Stacked PSB-only Spaxels

Type	Parameter	Form	Min	Max
SFH	$\log_{10} M_*/M_{\odot}$	Uniform	6	13
	$t_{\text{form}}$ (Gyr)	Uniform	4	14
	$\tau_e$ (Gyr)	Uniform	0.3	10
	$t_{\text{burst}}$ (Gyr)	Uniform	0	4
	$\alpha$	$\log_{10}$ uniform	0.01	1000
	$\beta$	Fixed = 250	...	...
Metallicity	$Z_{\text{old}}/Z_{\odot}$	$\log_{10}$ uniform	0.01	2.5
	$Z_{\text{burst}}/Z_{\odot}$	$\log_{10}$ Uniform	0.01	2.5
Dust	$A_V$	Uniform	0	2
	Birthcloud factor $\eta$	Uniform	1	5
GP noise	Uncorrelated amplitude $s$	$\log_{10}$ uniform	0.1	10
	Correlated amplitude $\sigma$	$\log_{10}$ uniform	$10^{-4}$	1
	Period/length scale $\rho$	$\log_{10}$ uniform	0.04	1
	Dampening quality factor $Q$	Fixed = 0.49	...	...
Miscellaneous	Redshift	Uniform	$0.8 z$	$1.2 z$
	$t_{\text{birth cloud}}$ (Gyr)	Fixed = 0.01	...	...
	$\sigma_{\text{disp}}$ ( $\text{km s}^{-1}$ )	$\log_{10}$ uniform	40	4000

**Note.** The SFH parameter symbols are described in Equations (2) and (3); the GP parameter symbols are described in Foreman-Mackey et al. (2017), Foreman-Mackey (2018), and H. Leung et al. (2022, in preparation). Other symbols have their usual meanings. A  $\log_{10}$  uniform prior form indicates a flat prior in  $\log(X) \sim U(\log(\text{min}), \log(\text{max}))$ . Redshift is given a uniform prior from 80%–120% of the target’s catalog value.

galaxies were to have a subsolar metallicity of  $Z' = 0.5$ , we find a mean  $\alpha_{\text{CO}} = 4.75 M_{\odot} (\text{K km s}^{-1} \text{pc}^2)^{-1}$ , thus slightly increasing our measured gas masses, but well within our uncertainties. A subsolar metallicity could be achieved from pristine gas inflow.

In Figure 14, we plot the gas fraction and SFE of our PSB regions (as in Figure 9) but with the variable  $\alpha_{\text{CO}}$  computed with Equation (C1), assuming  $Z' = 2$ . Though the gas fractions are lower and SFEs higher than with the Milky Way  $\alpha_{\text{CO}}$  as shown in Figure 9, our primary conclusion that many of our PSB regions have similar molecular gas fractions to the star-forming galaxies with lower SFEs still holds.

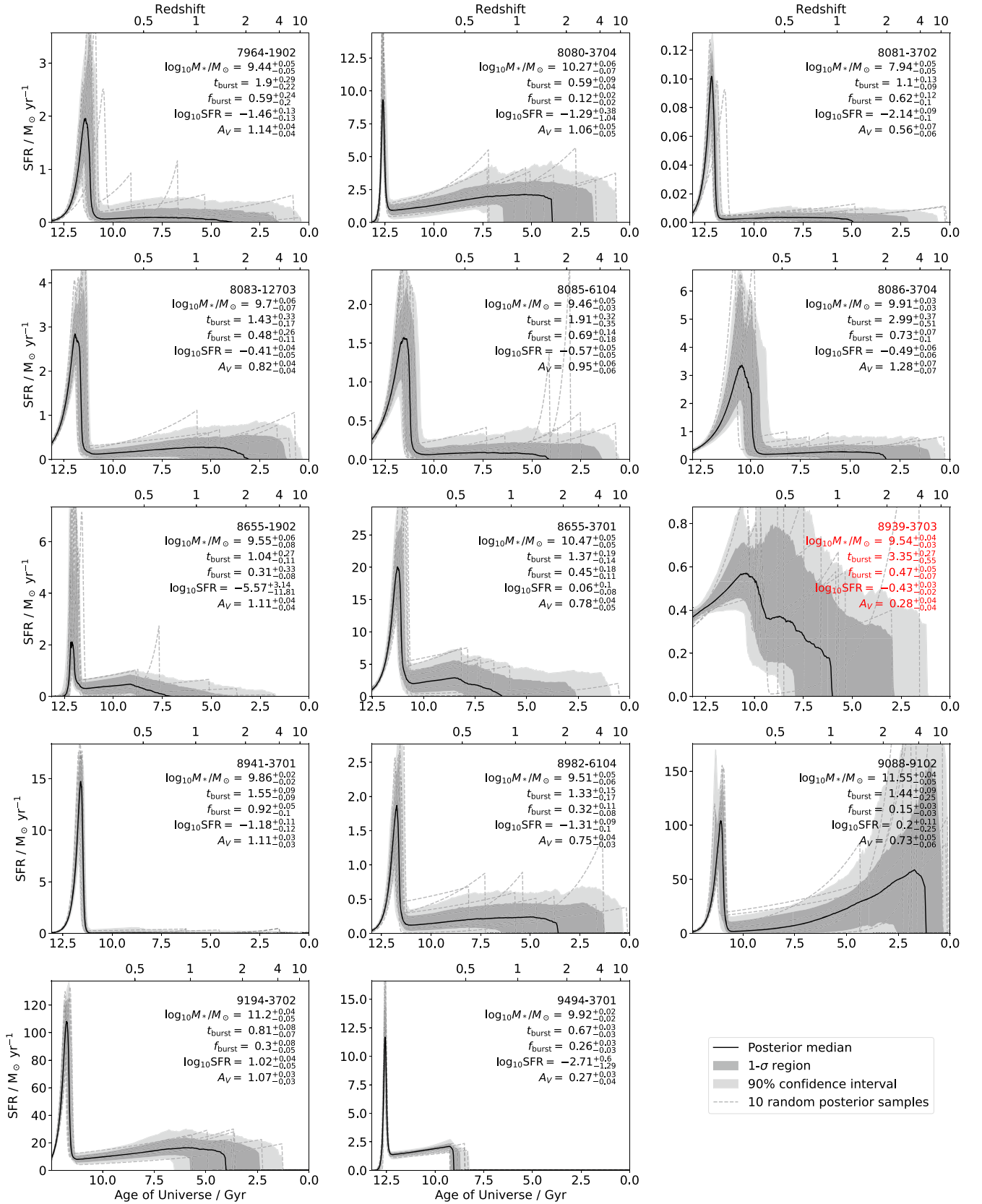


**Figure 15.** A montage of fitted SFHs through our spectral fitting methods (Section 3.2). In each panel, the MaNGA Plate-IFU, along with several key fitted properties (of only the PSB regions) are listed toward the top right. Their symbols correspond to those in Tables 5 and 3. 8939-3703, highlighted with red text, is found to be a star-forming interloper (see Appendix B). The bottom x-axis traces the age of the universe, with the corresponding redshift scale displayed on the top edge, while the y-axis shows SFRs. The SFHs grow progressively more uncertain with greater lookback time.

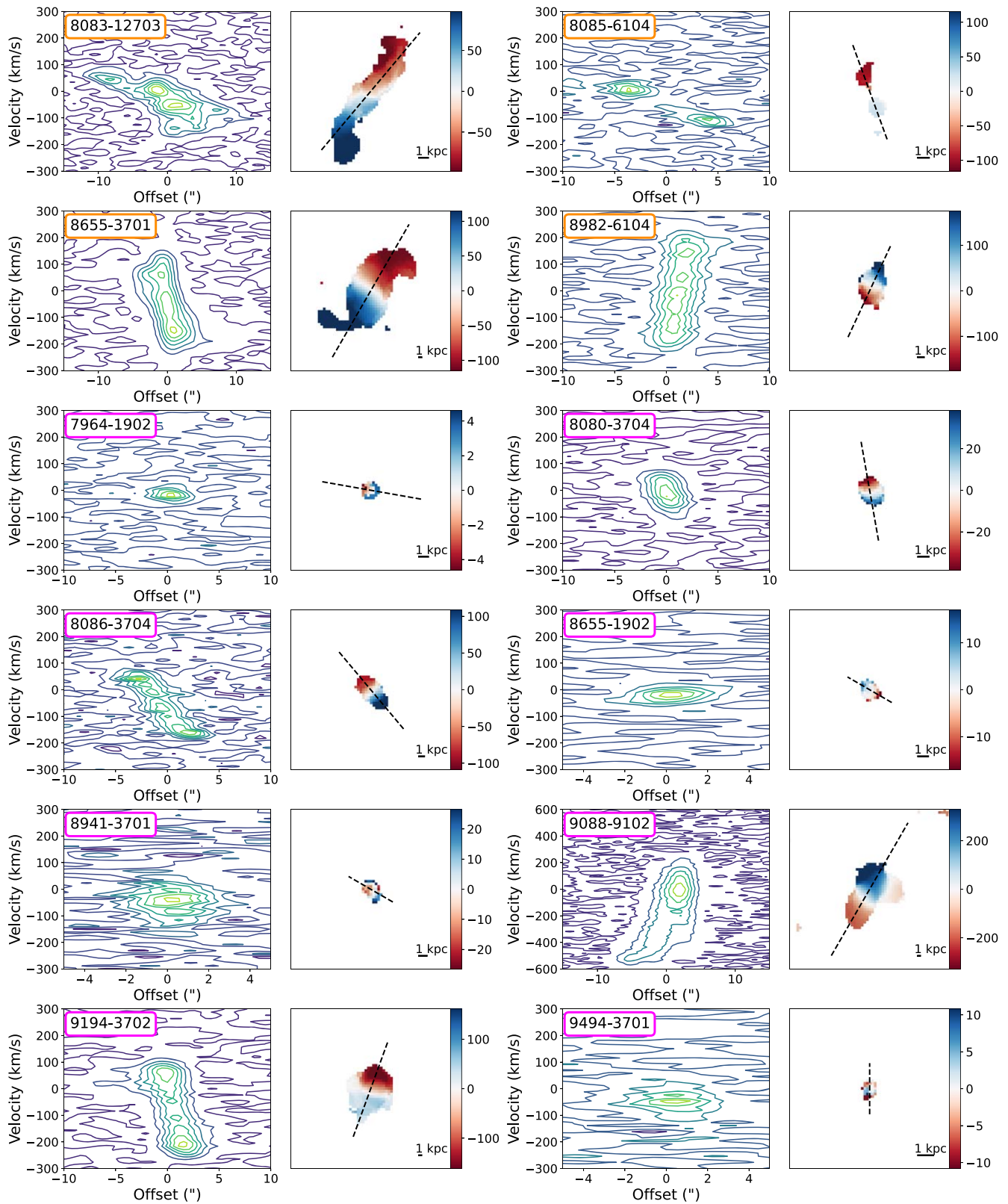


**Figure 16.** CO  $P$ - $V$  diagrams for each galaxy with a CO detection. The right panel shows the CO velocity field with a dashed line showing the axis where the  $P$ - $V$  diagram on the left is extracted from. The color bar is in units of kilometers per second.

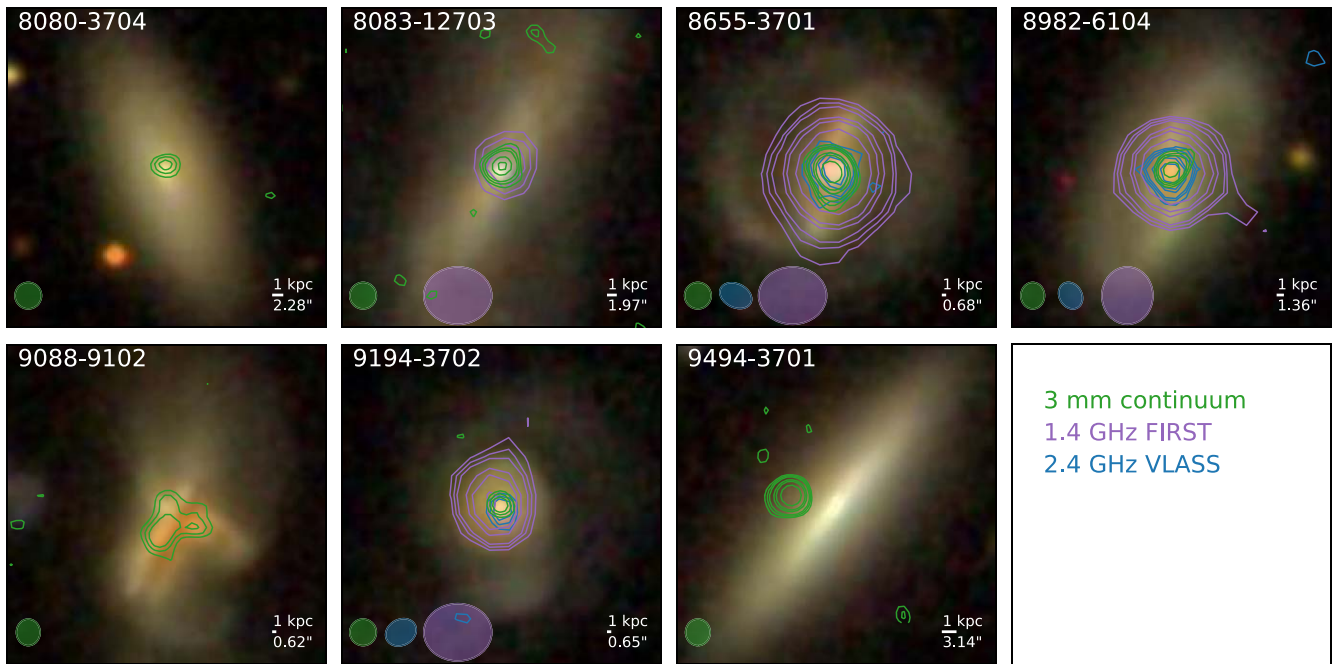


**Figure 17.** Millimeter and radio emission contours overlaid on SDSS 3-color images for galaxies with  $5\sigma$  millimeter or radio continuum detections. Green contours show the 3 mm continuum emission, purple contours show the FIRST 1.4 GHz emission, and blue contours show the VLASS 2.4 GHz emission. The ellipses in the lower left of each panel show the beam sizes with the same colors as the contours. Cutout images from the VLASS survey were accessed with `astroquery` (Ginsburg et al. 2019).

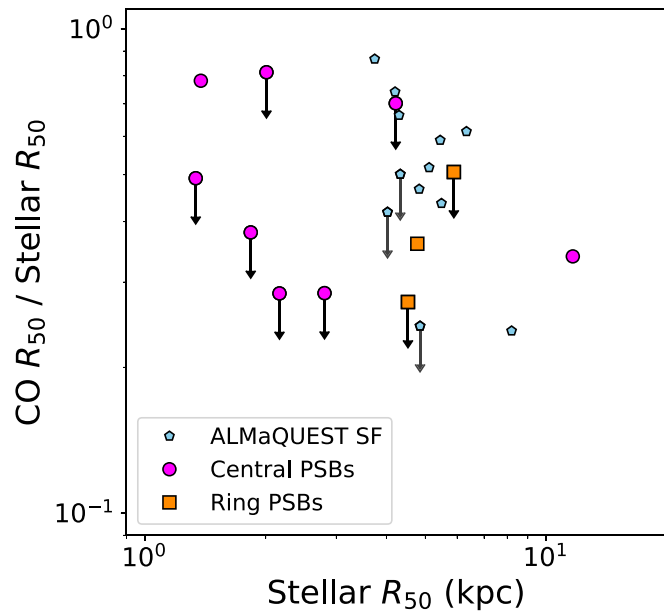


**Figure 18.** CO half-light radii and stellar  $r$ -band half-light radii for our PSB sample (centrals in purple, rings in pink) and star-forming galaxies (blue). Galaxies with greater than 50% of CO emission from the central  $3\sigma$  of the beam are upper limits.

#### Appendix D Fitting SFHs

Table 5 lists the 18 parameters in the final SFH model, with 15 free to vary with priors. The parameters are described in Section 3.2.

Figure 15 shows our derived SFHs for each galaxy in our sample. The spectral fitting methods used are described in Section 3.2. SFH parameters such as the time since burst, burst mass fraction, etc. are listed for each galaxy in Table 3.

#### Appendix E $P$ - $V$ Diagrams

In Figure 16, we plot the CO  $P$ - $V$  diagram for each galaxy with a CO detection. We select the axis along which we extract the  $P$ - $V$  diagram by hand with a width of  $1''$ . We see that six galaxies have rotating CO emission, though these galaxies do not have a flattening of their rotation curves at larger radii, possibly as a result of the centrally concentrated gas morphologies. One galaxy has a bar, 8655-3701, as shown by the “X” shape in the  $P$ - $V$  diagram. This galaxy also has an obvious stellar bar in the optical image. Finally, the  $P$ - $V$  diagram of 8083-12703 shows a complex kinematic structure with a radius-dependent kinematic position angle, which may be indicative of some disturbance such as a minor merger or interaction.

#### Appendix F 3 mm and Radio Continuum Detections

Radio and millimeter continuum detections can be associated with an AGN or a starburst (e.g., Best et al. 2005). We detect 3 mm continuum emission to  $5\sigma$  in 7/13 of our PSB galaxies. For each galaxy, this emission is unresolved and in the center of the galaxy except for 9088-9102, which has extended continuum emission in the center, and 9494-3701, which has continuum emission offset from the center.

We measure radio fluxes of our galaxies from cutouts from the VLA Sky Survey (VLASS; Lacy et al. 2020) and Faint Images of the Radio Sky at Twenty centimeters survey (FIRST; Becker et al. 1994) at the optical source locations of our galaxies. We first fit the cutouts with a 2D Gaussian, and measure fluxes within an elliptical aperture corresponding to the  $3\sigma$  Gaussian fit size. We measure four galaxies with  $S/N > 3$  from the FIRST survey, and three from VLASS. We show the 3 mm continuum contours for galaxies with a  $5\sigma$



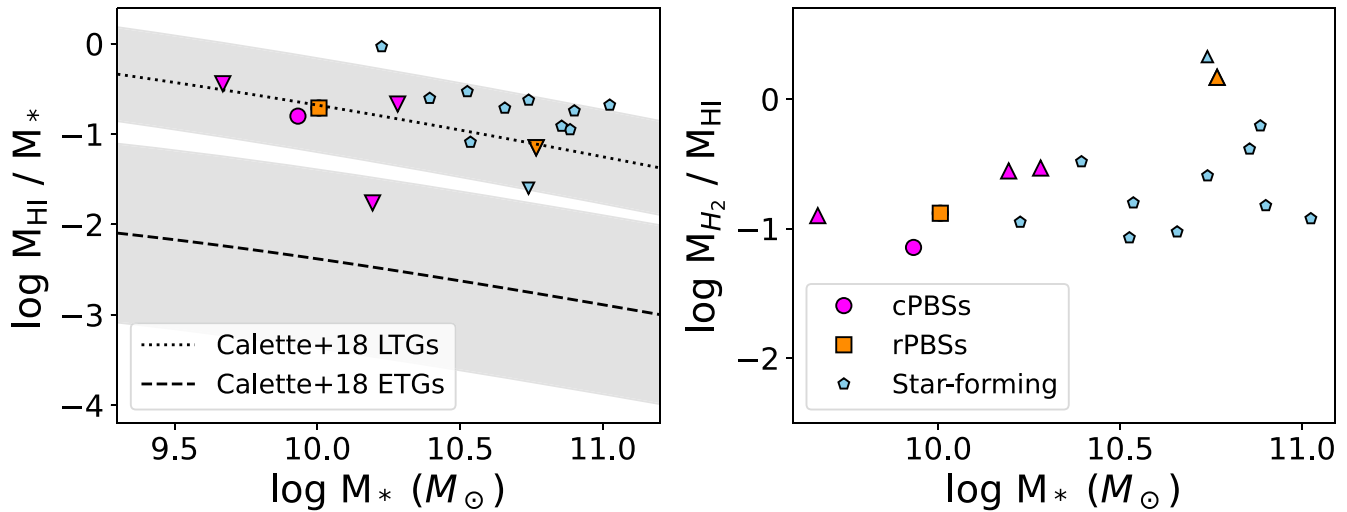


**Figure 19.** Left: H I gas fraction ( $M_{\text{HI}}/M_*$ ) vs. stellar mass for our cPSB galaxies in purple, rPSB galaxies in orange, and the ALMaQUEST star-forming galaxies in blue. Downward-pointing triangles represent  $M_{\text{HI}}$  upper limits. The dotted and dashed lines show the double power-law fits for LTGs and ETGs from Calette et al. (2018), respectively. Right: molecular-to-atomic gas ratio ( $M_{\text{H}_2}/M_{\text{HI}}$ ) vs. stellar mass for the same samples. Upward arrows show  $M_{\text{HI}}$  upper limits, and downward-pointing arrows show the  $M_{\text{H}_2}$  upper limits.

continuum millimeter or radio detection, overlaid on the 3-color SDSS image in Figure 17. For galaxies with radio continuum detections, the emission is co-incident with the millimeter continuum emission.

For the majority of 3 mm continuum detected galaxies, AGN likely contributes to the 3 mm emission, though star formation may also contribute significantly as a dust heating source and through free-free emission. Of the seven galaxies with 3 mm continuum emission, five have central emission line ratios consistent with some AGN contribution (see Section 4.5). 8083-12703 is an rPSB with 3 mm emission and no evidence of a central AGN but does have a star-forming center, indicating that the central, compact 3 mm emission could be from a central starburst. The extended nature of the 3 mm emission in 9088-9102 also points toward a significant contribution from star formation, as we would expect continuum emission heated by a central AGN to be highly compact. Lastly, the offset of the continuum emission of 9494-3701 and the optical center of the galaxy indicates that this emission may be from a background source rather than from within the galaxy itself. None of the 12 ALMaQUEST star-forming galaxies have 3 mm continuum detections.

### Appendix G Half-light Radii

We use the `statmorph` python code to measure the half-light radii of the CO emission for our PSB galaxies and the star-forming ALMaQUEST galaxies (Rodríguez-Gomez et al. 2019). We use the half-light radius to measure the overall extent of the CO rather than the central core size measured by the 2D Gaussian fit. We input a segmentation map of the largest contiguous region of spaxels with  $3\sigma$  CO detections. We plot the CO and  $r$ -band half-light radii in Figure 18. Galaxies with  $f_{\text{core}} \geq 50\%$  are upper limits because at least half of their CO emission is unresolved. While some of our PSB galaxies cannot be distinguished from the star-forming galaxies due to loosely constraining CO size upper limits, we see that the molecular gas of PSB galaxies is at least as compact as the







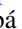







most compact ALMaQUEST star-forming galaxies, relative to the  $r$ -band effective radius.

### Appendix H H I Gas Properties

We investigate the H I properties of our sample with data from the H I-MaNGA survey (Stark et al. 2021), a MaNGA follow-up survey of H I observations with the Green Bank Telescope. We only include galaxies that have a source confusion probability less than 10%. Of our 13 PSB galaxies, 10 were observed (the other three are outside the redshift cut of  $z < 0.05$ ), and 6/10 were detected. Only 2/6 detected PSB galaxies have sufficiently low confusion probabilities, 7964-1902 and 8085-6104. We plot the H I gas fractions ( $M_{\text{HI}}/M_*$ ) and  $\text{H}_2$  to H I mass ratio for our PSB galaxies and the ALMaQUEST star-forming galaxies in Figure 19. We also show the measured H I gas fraction and stellar mass double power-law relations for LTGs and ETGs from Calette et al. (2018). The two H I-detected PSB galaxies have similar H I gas fractions as the star-forming galaxies, and similar  $\text{H}_2$  to H I mass ratios. One PSB, 9494-3701, with an H I mass upper limit has a low H I gas fraction consistent with the ETGs of Calette et al. (2018). With only two H I detections in our sample, higher resolution H I observations are needed to understand the atomic gas content of our PSB galaxies, especially those with nearby galaxies where source confusion is an issue.

### ORCID iDs

Justin Atsushi Otter <https://orcid.org/0000-0003-3191-9039>  
 Kate Rowlands <https://orcid.org/0000-0001-7883-8434>  
 Katherine Alatalo <https://orcid.org/0000-0002-4261-2326>  
 Ho-Hin Leung <https://orcid.org/0000-0003-0486-5178>  
 Vivienne Wild <https://orcid.org/0000-0002-8956-7024>  
 Yuanze Luo <https://orcid.org/0000-0002-0696-6952>  
 Andreea O. Petric <https://orcid.org/0000-0003-4030-3455>  
 Elizaveta Sazonova <https://orcid.org/0000-0001-6245-5121>  
 Timothy Heckman <https://orcid.org/0000-0001-6670-6370>  
 Timothy A. Davis <https://orcid.org/0000-0003-4932-9379>  
 Sara Ellison <https://orcid.org/0000-0002-1768-1899>

K. Decker French  <https://orcid.org/0000-0002-4235-7337>  
 William Baker  <https://orcid.org/0000-0003-0215-1104>  
 Asa F. L. Bluck  <https://orcid.org/0000-0001-6395-4504>  
 Lauranne Lanz  <https://orcid.org/0000-0002-3249-8224>  
 Lihwai Lin  <https://orcid.org/0000-0001-7218-7407>  
 Charles Liu  <https://orcid.org/0000-0002-4314-8713>  
 Carlos López Cobá  <https://orcid.org/0000-0003-1045-0702>  
 Karen L. Masters  <https://orcid.org/0000-0003-0846-9578>  
 Hsi-an Pan  
 (潘璽安)  <https://orcid.org/0000-0002-1370-6964>  
 Rogemar A. Riffel  <https://orcid.org/0000-0003-0483-3723>  
 Jillian M. Scudder  <https://orcid.org/0000-0002-8798-3972>  
 Adam Smercina  <https://orcid.org/0000-0003-2599-7524>  
 Freeke van de Voort  <https://orcid.org/0000-0002-6301-638X>  
 John R. Weaver  <https://orcid.org/0000-0003-1614-196X>

## References

- Aalto, S., Garcia-Burillo, S., Muller, S., et al. 2015, *A&A*, 574, A85  
 Aguado, D. S., Ahumada, R., Almeida, A., et al. 2019, *ApJS*, 240, 23  
 Alatalo, K., Appleton, P. N., Lisenfeld, U., et al. 2014, *ApJ*, 795, 159  
 Alatalo, K., Appleton, P. N., Lisenfeld, U., et al. 2015a, *ApJ*, 812, 117  
 Alatalo, K., Lacy, M., Lanz, L., et al. 2015b, *ApJ*, 798, 31  
 Alatalo, K., Bitsakis, T., Lanz, L., et al. 2017, *ApJ*, 843, 9  
 Alatalo, K., Blitz, L., Young, L. M., et al. 2011, *ApJ*, 735, 88  
 Alatalo, K., Cales, S. L., Rich, J. A., et al. 2016a, *ApJS*, 224, 38  
 Alatalo, K., Lisenfeld, U., Lanz, L., et al. 2016b, *ApJ*, 827, 106  
 Astropy Collaboration, Price-Whelan, A. M., Sipőcz, B. M., et al. 2018, *AJ*, 156, 123  
 Astropy Collaboration, Robitaille, T. P., Tollerud, E. J., et al. 2013, *A&A*, 558, A33  
 Athanassoula, E. 1992, *MNRAS*, 259, 345  
 Athanassoula, E., Machado, R. E. G., & Rodionov, S. A. 2013, *MNRAS*, 429, 1949  
 Baldry, I. K., Glazebrook, K., Brinkmann, J., et al. 2004, *ApJ*, 600, 681  
 Baldwin, J. A., Phillips, M. M., & Terlevich, R. 1981, *PASP*, 93, 5  
 Baron, D., Netzer, H., Poznanski, D., Prochaska, J. X., & Förster Schreiber, N. M. 2017, *MNRAS*, 470, 1687  
 Becker, R. H., White, R. L., Helfand, D. J., & Zoonematkermani, S. 1994, *ApJS*, 91, 347  
 Bekki, K. 1998, *ApJ*, 502, L133  
 Bekki, K., Couch, W. J., & Shioya, Y. 2002, *ApJ*, 577, 651  
 Belfiore, F., Westfall, K. B., Schaefer, A., et al. 2019, *AJ*, 158, 160  
 Bell, E. F., van der Wel, A., Papovich, C., et al. 2012, *ApJ*, 753, 167  
 Bell, E. F., Zheng, X. Z., Papovich, C., et al. 2007, *ApJ*, 663, 834  
 Best, P. N., Kauffmann, G., Heckman, T. M., & Ivezić, Ž. 2005, *MNRAS*, 362, 9  
 Blanton, M. R., Bershady, M. A., Abolfathi, B., et al. 2017, *AJ*, 154, 28  
 Blanton, M. R., & Moustakas, J. 2009, *ARA&A*, 47, 159  
 Bluck, A. F. L., Maiolino, R., Sánchez, S. F., et al. 2020, *MNRAS*, 492, 96  
 Bolatto, A. D., Wolfire, M., & Leroy, A. K. 2013, *ARA&A*, 51, 207  
 Bruzual, G., & Charlot, S. 2003, *MNRAS*, 344, 1000  
 Buchner, J., Georgakakis, A., Nandra, K., et al. 2014, *A&A*, 564, A125  
 Bundy, K., Bershady, M. A., Law, D. R., et al. 2014, *ApJ*, 798, 7  
 Calette, A. R., Avila-Reese, V., Rodríguez-Puebla, A., Hernández-Toledo, H., & Papastergis, E. 2018, *RMxAA*, 54, 443  
 Cappellari, M., Emsellem, E., Krajnović, D., et al. 2011, *MNRAS*, 413, 813  
 Carnall, A. C., McLure, R. J., Dunlop, J. S., et al. 2019, *MNRAS*, 490, 417  
 Carnall, A. C., McLure, R. J., Dunlop, J. S., & Davé, R. 2018, *MNRAS*, 480, 4379  
 Chen, Y.-M., Shi, Y., Wild, V., et al. 2019, *MNRAS*, 489, 5709  
 Cherinka, B., Andrews, B. H., Sánchez-Gallego, J., et al. 2019, *AJ*, 158, 74  
 Chung, A., van Gorkom, J. H., Kenney, J. D. P., Crowl, H., & Vollmer, B. 2009, *AJ*, 138, 1741  
 Cicone, C., Maiolino, R., Sturm, E., et al. 2014, *A&A*, 562, A21  
 Cid Fernandes, R., Stasińska, G., Mateus, A., & Vale Asari, N. 2011, *MNRAS*, 413, 1687  
 Ciotti, L., Ostriker, J. P., & Proga, D. 2010, *ApJ*, 717, 708  
 Davis, T. A., Alatalo, K., Sarzi, M., et al. 2011, *MNRAS*, 417, 882  
 Davis, T. A., van de Voort, F., Rowlands, K., et al. 2019, *MNRAS*, 484, 2447  
 de los Reyes, M. A. C., & Kennicutt, R. C., Jr. 2019, *ApJ*, 872, 16  
 Drory, N., MacDonald, N., Bershady, M. A., et al. 2015, *AJ*, 149, 77  
 Ellison, S. L., Thorp, M. D., Pan, H.-A., et al. 2020, *MNRAS*, 492, 6027  
 Falcón-Barroso, J., Sánchez-Blázquez, P., Vazdekis, A., et al. 2011, *A&A*, 532, A95  
 Federrath, C., & Klessen, R. S. 2012, *ApJ*, 761, 156  
 Feigelson, E. D., & Babu, G. J. 2012, *Modern Statistical Methods for Astronomy: With R Applications* (Cambridge: Cambridge Univ. Press)  
 Feroz, F., & Hobson, M. P. 2008, *MNRAS*, 384, 449  
 Feruglio, C., Maiolino, R., Piconcelli, E., et al. 2010, *A&A*, 518, L155  
 Foreman-Mackey, D. 2018, *RNAAS*, 2, 31  
 Foreman-Mackey, D., Agol, E., Ambikasaran, S., & Angus, R. 2017, *AJ*, 154, 220  
 Fraser-McKelvie, A., Aragón-Salamanca, A., Merrifield, M., et al. 2020, *MNRAS*, 495, 4158  
 French, K. D. 2021, *PASP*, 133, 072001  
 French, K. D., Yang, Y., Zabludoff, A., et al. 2015, *ApJ*, 801, 1  
 French, K. D., Yang, Y., Zabludoff, A. I., & Tremonti, C. A. 2018, *ApJ*, 862, 2  
 Gensior, J., & Kruijssen, J. M. D. 2021, *MNRAS*, 500, 2000  
 George, K., Joseph, P., Mondal, C., et al. 2019, *A&A*, 621, L4  
 Géron, T., Smethurst, R. J., Lintott, C., et al. 2021, *MNRAS*, 507, 4389  
 Ginsburg, A., Sipőcz, B. M., Brasseur, C. E., et al. 2019, *AJ*, 157, 98  
 Goto, T. 2007, *MNRAS*, 377, 1222  
 Goto, T., Nichol, R. C., Okamura, S., et al. 2003, *PASJ*, 55, 771  
 Greene, O. A., Anderson, M. R., Marinelli, M., et al. 2021, *ApJ*, 910, 162  
 Guillard, P., Boulanger, F., Lehnert, M. D., et al. 2015, *A&A*, 574, A32  
 Gunn, J. E., & Gott, J. R., III 1972, *ApJ*, 176, 1  
 Gunn, J. E., Siegmund, W. A., Mannery, E. J., et al. 2006, *AJ*, 131, 2332  
 Hamann, F., Korista, K. T., Ferland, G. J., Warner, C., & Baldwin, J. 2002, *ApJ*, 564, 592  
 Hauschik, R. W. 2003, *A&A*, 407, 1157  
 Hao, C.-N., Kennicutt, R. C., Johnson, B. D., et al. 2011, *ApJ*, 741, 124  
 Harris, C. R., Millman, K. J., van der Walt, S. J., et al. 2020, *Natur*, 585, 357  
 Heckman, T. M., Armus, L., & Miley, G. K. 1990, *ApJS*, 74, 833  
 Hunter, J. D. 2007, *CSE*, 9, 90  
 Ilbert, O., McCracken, H. J., Le Fèvre, O., et al. 2013, *A&A*, 556, A55  
 Jin, S.-W., Gu, Q., Huang, S., Shi, Y., & Feng, L.-L. 2014, *ApJ*, 787, 63  
 Kauffmann, G., Heckman, T. M., Tremonti, C., et al. 2003a, *MNRAS*, 346, 1055  
 Kauffmann, G., Heckman, T. M., White, S. D. M., et al. 2003b, *MNRAS*, 341, 54  
 Kaviraj, S., Kirkby, L. A., Silk, J., & Sarzi, M. 2007, *MNRAS*, 382, 960  
 Kennicutt, R. C., Jr. 1998, *ApJ*, 498, 541  
 Kewley, L. J., Dopita, M. A., Sutherland, R. S., Heisler, C. A., & Trevena, J. 2001, *ApJ*, 556, 121  
 Kewley, L. J., Groves, B., Kauffmann, G., & Heckman, T. 2006, *MNRAS*, 372, 961  
 Kewley, L. J., Nicholls, D. C., & Sutherland, R. S. 2019, *ARA&A*, 57, 511  
 Krajnović, D., Cappellari, M., de Zeeuw, P. T., & Copin, Y. 2006, *MNRAS*, 366, 787  
 Kroupa, P. 2001, *MNRAS*, 322, 231  
 Kruk, S. J., Lintott, C. J., Bamford, S. P., et al. 2018, *MNRAS*, 473, 4731  
 Krumholz, M. R., Dekel, A., & McKee, C. F. 2012, *ApJ*, 745, 69  
 Krumholz, M. R., & McKee, C. F. 2005, *ApJ*, 630, 250  
 Kumari, N., Maiolino, R., Trussler, J., et al. 2021, *A&A*, 656, A140  
 Lacy, M., Baum, S. A., Chandler, C. J., et al. 2020, *PASP*, 132, 035001  
 Law, D. R., Yan, R., Bershady, M. A., et al. 2015, *AJ*, 150, 19  
 Li, Z., French, K. D., Zabludoff, A. I., & Ho, L. C. 2019, *ApJ*, 879, 131  
 Lin, L., Ellison, S. L., Pan, H.-A., et al. 2020, *ApJ*, 903, 145  
 Lin, L., Ellison, S. L., Pan, H.-A., et al. 2022, *ApJ*, 926, 175  
 Lin, L., Pan, H.-A., Ellison, S. L., et al. 2019, *ApJL*, 884, L33  
 Lotz, J. M., Primack, J., & Madau, P. 2004, *AJ*, 128, 163  
 Luo, Y., Rowlands, K., Alatalo, K., et al. 2022, *ApJ*, 938, 63  
 Martig, M., Bournaud, F., Teyssier, R., & Dekel, A. 2009, *ApJ*, 707, 250  
 Martig, M., Crocker, A. F., Bournaud, F., et al. 2013, *MNRAS*, 432, 1914  
 McMullin, J. P., Waters, B., Schiebel, D., Young, W., & Golap, K. 2007, in *ASP Conf. Ser. 376, Astronomical Data Analysis Software and Systems XVI*, ed. R. A. Shaw, F. Hill, & D. J. Bell (San Francisco, CA: ASP), 127  
 Mihos, J. C. 1995, *ApJL*, 438, L75  
 Moore, B., Katz, N., Lake, G., Dressler, A., & Oemler, A. 1996, *Natur*, 379, 613  
 Murray, N. 2011, *ApJ*, 729, 133  
 Narayanan, D., Krumholz, M., Ostriker, E. C., & Hernquist, L. 2011, *MNRAS*, 418, 664  
 Narayanan, D., Krumholz, M. R., Ostriker, E. C., & Hernquist, L. 2012, *MNRAS*, 421, 3127  
 Owers, M. S., Hudson, M. J., Oman, K. A., et al. 2019, *ApJ*, 873, 52

- Pace, Z. J., Tremonti, C., Chen, Y., et al. 2019, *ApJ*, 883, 83
- Pawlik, M. M., Taj Aldeen, L., Wild, V., et al. 2018, *MNRAS*, 477, 1708
- Piotrowska, J. M., Bluck, A. F. L., Maiolino, R., & Peng, Y. 2021, *MNRAS*, 512, 1052
- Querejeta, M., Meidt, S. E., Schinnerer, E., et al. 2016, *A&A*, 588, A33
- Regan, M. W., Vogel, S. N., & Teuben, P. J. 1997, *ApJL*, 482, L143
- Rodríguez-Gomez, V., Snyder, G. F., Lotz, J. M., et al. 2019, *MNRAS*, 483, 4140
- Rowlands, K., Heckman, T., Wild, V., et al. 2018, *MNRAS*, 480, 2544
- Rowlands, K., Wild, V., Nesvadba, N., et al. 2015, *MNRAS*, 448, 258
- Salim, D. M., Alatalo, K., Federrath, C., Groves, B., & Kewley, L. J. 2020, *ApJ*, 893, 26
- Sazonova, E., Alatalo, K., Rowlands, K., et al. 2021, *ApJ*, 919, 134
- Schawinski, K., Urry, C. M., Simmons, B. D., et al. 2014, *MNRAS*, 440, 889
- Scoville, N., Murchikova, L., Walter, F., et al. 2017, *ApJ*, 836, 66
- Smee, S. A., Gunn, J. E., Uomoto, A., et al. 2013, *AJ*, 146, 32
- Smercina, A., Smith, J. D. T., Dale, D. A., et al. 2018, *ApJ*, 855, 51
- Smercina, A., Smith, J.-D. T., French, K. D., et al. 2022, *ApJ*, 929, 154
- Stark, D. V., Bundy, K. A., Westfall, K., et al. 2018, *MNRAS*, 480, 2217
- Stark, D. V., Masters, K. L., Avila-Reese, V., et al. 2021, *MNRAS*, 503, 1345
- Thorp, M. D., Ellison, S. L., Simard, L., Sánchez, S. F., & Antonio, B. 2019, *MNRAS Lett.*, 482, L55
- Vera, M., Alonso, S., & Coldwell, G. 2016, *A&A*, 595, A63
- Wake, D. A., Bundy, K., Diamond-Stanic, A. M., et al. 2017, *AJ*, 154, 86
- Westfall, K. B., Cappellari, M., Bershady, M. A., et al. 2019, *AJ*, 158, 231
- Wild, V., Kauffmann, G., Heckman, T., et al. 2007, *MNRAS*, 381, 543
- Wild, V., Taj Aldeen, L., Carnall, A., et al. 2020, *MNRAS*, 494, 529
- Wild, V., Walcher, C. J., Johansson, P. H., et al. 2009, *MNRAS*, 395, 144
- Wilkinson, C. L., Pimblet, K. A., Stott, J. P., Few, C. G., & Gibson, B. K. 2018, *MNRAS*, 479, 758
- Yan, R., Newman, J. A., Faber, S. M., et al. 2006, *ApJ*, 648, 281
- Yan, R., Newman, J. A., Faber, S. M., et al. 2009, *MNRAS*, 398, 735
- Yan, R., Tremonti, C., Bershady, M. A., et al. 2015, *AJ*, 151, 8
- Yang, Y., Zabludoff, A. I., Zaritsky, D., & Mihos, J. C. 2008, *ApJ*, 688, 945
- Yesuf, H. M., French, K. D., Faber, S. M., & Koo, D. C. 2017, *MNRAS*, 469, 3015
- Young, L. M., Bureau, M., Davis, T. A., et al. 2011, *MNRAS*, 414, 940
- Zheng, Y., Wild, V., Lahén, N., et al. 2020, *MNRAS*, 498, 1259